Nano Research Energy

ISSN 2791-0091 CN 10-1944/O6
https://doi.org/10.26599/NRE.2026.9120294

Research Article

Ni-induced Structural Spring Effect in High-performance Mn-Rich P2-Type Sodium Cathodes

Yangyang Huang[1,§], Qingyun Hu[2,§], Peng Wei[3](✉), Zhiwei Hu[4], Han Liu[2](✉), Yong Wang[5], Shiwen Wang[6], Pengcheng Wang[6], Linsen Li[5], Yang Ren[2], Zhanhua Wei[1](✉)

[1] Xiamen Key Laboratory of Optoelectronic Materials and Advanced Manufacturing, Institute of Luminescent Materials and Information Displays, College of Materials Science and Engineering, Huaqiao University, Xiamen 361000, China

[2] Department of Physics, JC STEM Lab of Energy and Materials Physics, City University of Hong Kong, Hong Kong 999077, China

[3] School of Materials Science and Engineering, Changzhou University, Changzhou 213164, China

[4] Max Planck Institute for Chemical Physics of Solids, Nöthnitzer Strasse 40, 01187, Dresden, Germany

[5] Department of Chemical Engineering, Shanghai Electrochemical Energy Devices Research Center, School of Chemistry and Chemical Engineering, Shanghai Jiao Tong University, Shanghai, China

[6] Xiamen Key Laboratory of Lithium Battery Energy Storage Application Materials and Safety, Xiamen Hithium Energy Storage Technology Co., Ltd., Xiamen 361000, China

[§] These authors contributed equally.

Nano Research Energy, **Just Accepted Manuscript** • https://doi.org/10.26599/NRE.2026.9120294
https://www.sciopen.com/journal/2791-0091 on Nov. 3, 2026

© The Authors(s)

Just Accepted

This is a "Just Accepted" manuscript, which has been examined by the peer-review process and has been accepted for publication. A "Just Accepted" manuscript is published online shortly after its acceptance, which is prior to technical editing and formatting and author proofing. Tsinghua University Press (TUP) provides "Just Accepted" as an optional and free service which allows authors to make their results available to the research community as soon as possible after acceptance. After a manuscript has been technically edited and formatted, and the page proofs have been corrected, it will be removed from the "Just Accepted" web site and published officially with volume and article number (e.g., Nano Research Energy, 2025, 4, e9120191). Please note that technical editing may introduce minor changes to the manuscript text and/or graphics which may affect the content, and all legal disclaimers that apply to the journal pertain. In no event shall TUP be held responsible for errors or consequences arising from the use of any information contained in these "Just Accepted" manuscripts. To cite this manuscript please use its Digital Object Identifier (DOI®), which is identical for all formats of publication.

Nano Research Energy

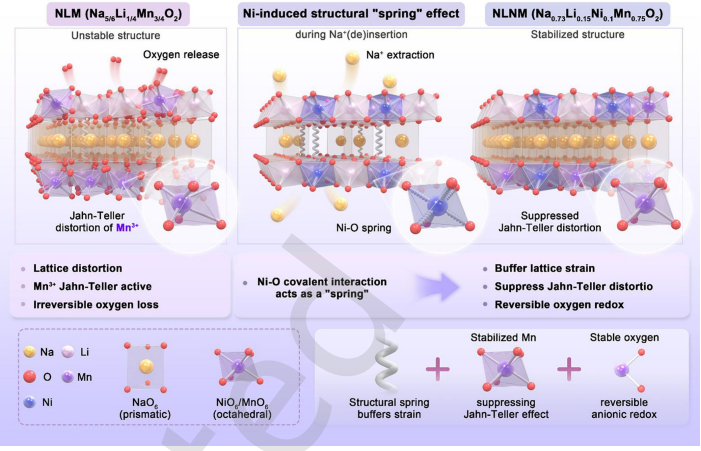
ISSN 2791-0091 (print); 2790-8119 (online)
https://doi.org/10.26599/NRE.2026.9120294

Table of Content

Ni-induced structural Spring Effect in high-performance Mn-Rich P2-Type Sodium Cathodes

Yangyang Huang[1‡], Qingyun Hu[2‡], Peng Wei[3]*, Zhiwei Hu[4], Han Liu[2]*, Yong Wang[5], Shiwen Wang[6], Pengcheng Wang[6], Linsen Li[5], Yang Ren[2] and Zhanhua Wei[1]*

1 Xiamen Key Laboratory of Optoelectronic Materials and Advanced Manufacturing, Institute of Luminescent Materials and Information Displays, College of Materials Science and Engineering, Huaqiao University, Xiamen 361000, China.
2 Department of Physics, JC STEM Lab of Energy and Materials Physics, City University of Hong Kong, Hong Kong 999077, China.
3 School of Materials Science and Engineering, Changzhou University, Changzhou 213164, China.
4 Max Planck Institute for Chemical Physics of Solids, Nöthnitzer Strasse 40, 01187, Dresden, Germany.
5 Department of Chemical Engineering, Shanghai Electrochemical Energy Devices Research Center, School of Chemistry and Chemical Engineering, Shanghai Jiao Tong University, Shanghai, China.
6 Xiamen Key Laboratory of Lithium Battery Energy Storage Application Materials and Safety, Xiamen Hithium Energy Storage Technology Co., Ltd., Xiamen 361000, China.



Ni-induced covalent strengthening acts as a structural spring to buffer lattice strain, suppress Jahn–Teller distortion, and stabilize reversible oxygen redox, enabling high-rate capability and prolonged cycling stability in P2-type Mn-rich layered cathodes.

Yangyang Huang, https://fgcl.hqu.edu.cn/info/1298/10104.htm
Peng Wei, https://clxy.cczu.edu.cn/2024/0407/c2589a358884/page.htm
Zhanhua Wei, https://fgcl.hqu.edu.cn/info/1298/3214.htm

Just Accepted

Research Article

Nano Research Energy

ISSN 2791-0091 (print); 2790-8119 (online)
https://doi.org/10.26599/NRE.2026.9120294

Research Article

Ni-induced Structural Spring Effect in High-performance Mn-Rich P2-Type Sodium Cathodes

Yangyang Huang[1,§], Qingyun Hu[2,§], Peng Wei[3] (✉), Zhiwei Hu[4], Han Liu[2] (✉), Yong Wang[5], Shiwen Wang[6], Pengcheng Wang[6], Linsen Li[5], Yang Ren[2], and Zhanhua Wei[1] (✉)

1 Xiamen Key Laboratory of Optoelectronic Materials and Advanced Manufacturing, Institute of Luminescent Materials and Information Displays, College of Materials Science and Engineering, Huaqiao University, Xiamen 361000, China.
2 Department of Physics, JC STEM Lab of Energy and Materials Physics, City University of Hong Kong, Hong Kong 999077, China.
3 School of Materials Science and Engineering, Changzhou University, Changzhou 213164, China.
4 Max Planck Institute for Chemical Physics of Solids, Nöthnitzer Strasse 40, 01187, Dresden, Germany.
5 Department of Chemical Engineering, Shanghai Electrochemical Energy Devices Research Center, School of Chemistry and Chemical Engineering, Shanghai Jiao Tong University, Shanghai, China.
6 Xiamen Key Laboratory of Lithium Battery Energy Storage Application Materials and Safety, Xiamen Hithium Energy Storage Technology Co., Ltd., Xiamen 361000, China.
§*These authors contributed equally.*

© The Author(s) 2026

Received: 2 September 2026 / **Revised:** 13 October 2026 / **Accepted:** 25 October 2026

ABSTRACT

Anionic redox chemistry offers a promising pathway toward high capacity in P2-type Mn-rich layered cathodes. However, the practical application is hindered by sluggish redox kinetics, severe oxygen loss, and structural deterioration, leading to poor cycling performance and particularly inadequate activity under high-current conditions. Herein, we propose a Ni-induced structural spring effect in P2-$Na_{5/6}Li_{1/4}Mn_{3/4}O_2$ (NLM) by partially substituting Li with Ni. This Ni-induced covalent strengthening acts as a structural "spring" that dynamically buffers mechanical stress during Na^+ extraction/insertion, effectively suppressing phase transitions at deep desodiation states and preserving structural integrity. Meanwhile, Ni incorporation effectively mitigates the Jahn–Teller distortion of Mn^{3+} by modulating the local coordination environment, thereby alleviating anisotropic lattice strain. Concurrently, the Ni–O octahedral spring effect bonding accelerates oxygen redox kinetics, mitigates voltage hysteresis, and suppresses irreversible oxygen release, thereby stabilizing the anionic redox activity at high rates. The resulting material, P2-$Na_{0.73}Li_{0.15}Ni_{0.1}Mn_{0.75}O_2$ (NLNM), exhibits nearly twofold reduction in overpotential during oxygen redox, delivers a specific capacity of ~150 mAh/g at the average voltage of 3.4 V, and retains 82% capacity after 200 cycles at 600 mA/g. This work demonstrates the strategy of Ni-induced spring effect for stable anionic activation and structural robustness, consequently achieving long-term cycling stability in high-performance oxide cathodes.

KEYWORDS

Sodium-ion batteries; P2-type layered oxide; Anionic redox; Spring effect; Jahn–Teller distortion

Just Accepted

© The Author(s) 2026. Published by Tsinghua University Press. The articles published in this open access journal are distributed under the terms of the Creative Commons Attribution 4.0 International License (http://creativecommons.org/licenses/by/4.0/), which permits use, distribution and reproduction in any medium, provided the original work is properly cited.

Address correspondence to Peng Wei, weipeng@cczu.edu.cn; Han Liu, hliu238@cityu.edu.hk; Zhanhua Wei, weizhanhua@hqu.edu.cn

TSINGHUA UNIVERSITY PRESS SciOpen

Nano Research Energy

ISSN 2791-0091 (print); 2790-8119 (online)
https://doi.org/10.26599/NRE.2026.9120294

1 Introduction

Owing to the abundance of sodium resources, low cost, and environmental friendliness, sodium-ion batteries (SIBs) are widely considered promising candidates for stationary energy storage [1-4]. Increasing the specific capacity of cathode materials is the critical goal for SIBs development to compensate for their intrinsic low energy density drawback compared to Li-ion batteries. Layered transition metal (TM) oxide cathodes have been studied due to their adjustable composition and high theoretical capacities [5, 6]. Given the introduction of cationic (Ni, Co, Mn, etc.) and anionic redox activity in Li-rich compounds [7, 8], the revolutionary anionic redox reactions are considered a new paradigm to deliver a higher capacity of similar cathodes for SIBs.

Commonly, anionic redox activity in layered TM oxide cathodes is triggered by introducing alkali metals into the TM slabs that generate the Na-O-A (A=Li, Na, Mg, vacancy) configurations with the oxygen lone pair electrons in the O 2p orbital [9-12]. Among these dopants, partial replacement of cations in TM layers with Li^+ to obtain a high anion capacity has been demonstrated [9, 13, 14]. Deep desodiation of Li-containing P2 cathodes can trigger TMO_2 slab gliding and the formation of O-type stacking faults or P/O intergrowth structures, which are closely coupled with irreversible Li/TM migration and oxygen loss, further deteriorating the structural reversibility [15]. Moreover, the initial charge/discharge specific capacity varies with varying Li/Mn ratios or working voltage ranges. Representatively, the typical P2-$Na_{5/6}Li_{1/4}Mn_{3/4}O_2$ with a high sodium content by optimizing the Li/Mn ratio was developed, delivering the charge/discharge capacity of approximately 175/190 mAh/g, respectively, in a voltage range of 1.5-4.5 V based on oxygen and Mn reduction. Unfortunately, such an anionic redox activity usually exhibits poor reversibility, accompanied by adverse oxygen release because of the high instability of oxidized O species [8, 16]. In addition, the lattice oxygen release can inevitably elicit the formation of the detrimental cation-dense phase and the related phase transformations [17]. Moreover, the intrinsically slow kinetics and asymmetric redox evolution of oxygen redox cause a large voltage hysteresis between charge and discharge, resulting in the low energy efficiency and poor rate capability of Mn-based layered oxide cathodes [18, 19]. To solve these problems, previous studies focused on the effects of anionic redox activity by inactive elements substitution and structural manipulation, including stacking, sequences of TM layer, cationic vacancies, and the superstructure-types of Li/Mn ordering [10, 20-24]. However, these studies have yet to address the kinetics of anionic redox chemistry, especially cycling at relatively high rates.

In this work, we introduce a novel Ni-induced structural spring effect in P2-type Mn-rich oxygen cathode via partially substituting Li with electrochemically active Ni, yielding a charge-balanced composition of $Na_{0.73}Li_{0.15}Ni_{0.1}Mn_{0.75}O_2$ (NLNM). As shown in Figure 1, the incorporation of Ni enhances TM–O covalency, which reinforces the surrounding Li–O bonds through Ni–O–Li configurations and accelerates oxygen redox kinetics and mitigates irreversible oxygen loss, thereby stabilizing anionic redox even under high rate conditions. This Ni-O bonding acts as a structural "spring" that dynamically buffers mechanical stress and mitigates the volume variation of the unit cell during Na+ extraction and insertion, suppressing detrimental phase transitions at deep desodiation states and preserving structural integrity. Ni incorporation also mitigates the Jahn–Teller distortion of Mn^{3+} by modulating the local coordination environment, alleviating the anisotropic lattice strain that typically deteriorates cycling stability. As a result, NLNM delivers a high discharge capacity of ~150 mAh/g with a high average operating voltage of 3.4 V and maintains 82% capacity after 200 cycles at a high current density of 600 mA/g. This work establishes a Ni-induced structural "spring effect" as a general design principle for coupling lattice dynamics with electronic structure to stabilize anionic redox and enhance structural robustness in next-generation sodium-ion batteries.

2 Results and Discussion

2.1 Structural and Morphological Characterization

P2-$Na_{0.83}Li_{0.25}Mn_{0.75}O_2$ (NLM) and P2-$Na_{0.73}Li_{0.15}Ni_{0.1}Mn_{0.75}O_2$ (NLNM) were prepared by a typical solid-state reaction method. The detailed preparation is described in the Experimental Section. Their crystal structures were characterized by X-ray diffraction (XRD). As shown in Figure 2a, the as-prepared samples belong to the P2-type structure with the *P*63/*mmc* space group. The (002) diffraction peak of NLNM shifts to a lower 2θ (inset of Figure 2a), suggesting that interlayer spacing is increased compared to NLM. The TM layer expansion indicates that Ni ions have successfully occupied the Li-sites since the ionic radius of Ni^{2+} (0.72 Å) is smaller than Li^+ (0.76 Å). Both XRD patterns of NLM and NLNM show a specific superstructure peak at approximately 2θ= 22.8°, which reflects the cationic ordering of Li/Mn in the TM layer [19]. This indicates that partial substitution of Li with Ni leads to the decreased intensity of this superstructure peak, indicating the weakening of the Li/Mn honeycomb ordered superlattice structure. The structure model of NLNM along the an axis is demonstrated in Figure 2b, which displays the composition of alternate Li/Ni/MnO_2 layers and Na layers with ABBA oxygen stacking patterns.

In terms of local structure, the traditional layered TM oxide cathodes, such as P2-$Na_xNi_{1/3}Mn_{2/3}O_2$ or O3-$NaNi_{1/3}Mn_{1/3}Fe_{1/3}O_2$, typically possess the 4TM-O-2Na configurations in their crystal structure (Figure 2c). In contrast, the configuration of the Li-incorporated Mn-based oxide cathodes with a long-range cation-ordered arrangement is 2TM-O-4Na/Li [18, 25, 26].

Just Accepted

Nano Research Energy
ISSN 2791-0091 (print); 2790-8119 (online)
https://doi.org/10.26599/NRE.2026.9120294

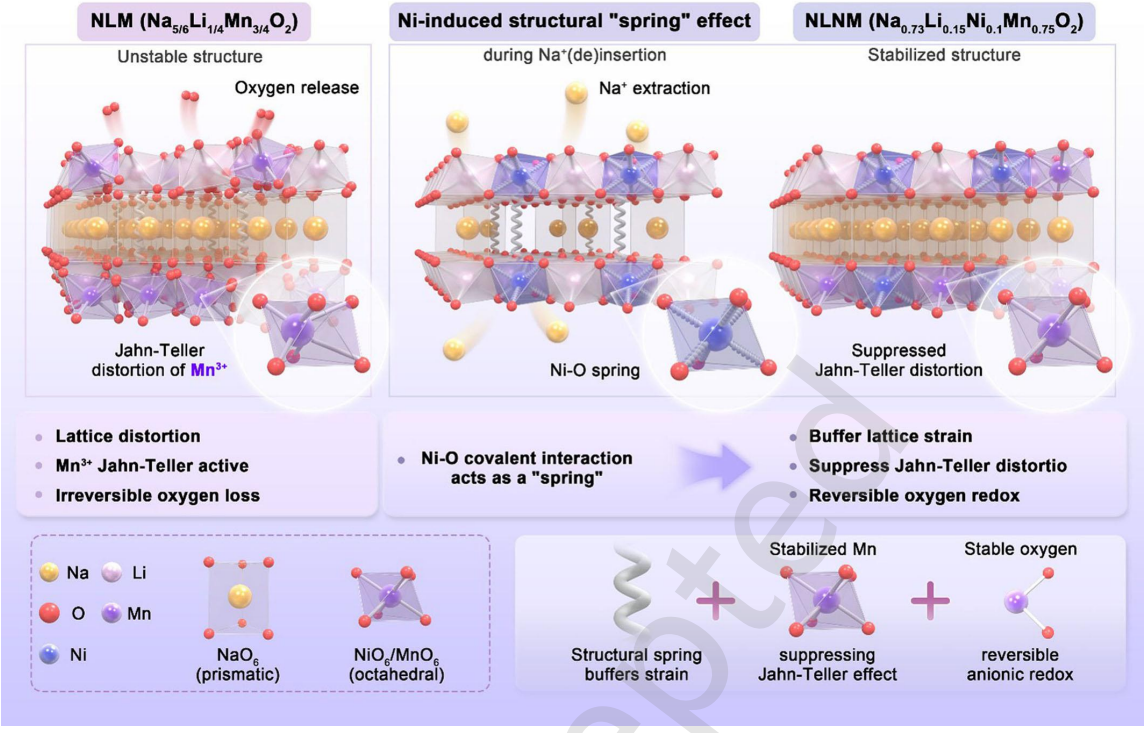


Figure 1 Schematic diagram of the Ni-induced structural "spring" effect in P2-NLM.

As the Ni substitution, the configuration transforms into a localized cation-disordered arrangement (3TM-O-3Na/Li or 4TM-O-2Na), similar to Li-rich oxide cathodes with gradually increasing Ni content [27]. The intensity reduction of the superlattice peak close to 22.8° can also reflect it. Furthermore, the XRD pattern of NLNM was fitted well using the hexagonal *P*63/*mmc* space group (Figure 2d). The refined lattice parameters are shown in Table S1. The *c*-axis parameter related to the TM layer distance of NLNM is 11.10 Å, which is larger than that of NLM (*c* = 11.04 Å) [28]. This is consistent with XRD results in Figure 2a.

As shown in Figure 2e, the Mn K-edge X-ray absorption near-edge structure (XANES) spectra of both NLM and NLNM are similar to MnO_2 reference, indicating the average Mn close to +4. The refined occupancies of Li, Ni, and Mn at the 2a site are 0.1493, 0.1014, and 0.7492, respectively, with a total occupancy close to unity, consistent with the nominal TM-layer composition of $Li_{0.15}Ni_{0.1}Mn_{0.75}$. The similar Mn K-edge positions of NLM and NLNM further indicate that Ni incorporation does not substantially alter the average Mn oxidation state. In addition, the K-edge spectra of NLNM slightly shift to low energy than that of LNM, which may cause by the substituting Li^+ by Ni^{2+}. The extended X-ray absorption fine structure (EXAFS) spectra (Figure S1) of NLNM shows a slight shift toward lower distance in the Mn-O bond than NLM, implying the local structure becomes more stable by Ni incorporation. X-ray photoelectron spectroscopy (XPS) characterization confirms that the calculated proportion of Mn^{3+} in NLNM is approximately 11% (Figure S2), consisting with the previous reports [9, 28]. Fourier transform (FT) of the Mn K-edge EXAFS, along with shell-by-shell fitting for NLNM (Figure 2g), reveals a slight shortening of the Mn-O bond to 1.893 Å, compared to 1.908 Å in NLM (Figure 2f). This indicates the enhanced local structural stability of the Mn-O coordination upon Ni incorporation. The HAADF-STEM image of NLNM in Figure 2h exhibits the plate-like morphology with inhomogeneous sizes from 1-5 μm. The energy dispersive spectroscopy (EDS) mapping images further confirms the homogeneous distribution of Mn and Ni, suggesting that Ni is uniformly incorporated into the lattice.

2.2 Electrochemical Performance

The half-cells were assembled to evaluate the electrochemical performance of NLM and NLNM. The normalized 1st and 5th charge/discharge profiles of NLM and NLNM can be shown in Figure 3a, b. There is a long slope from ~3.8 to 4.5 V and an S-shaped discharge profile in NLM. In contrast, NLNM displays a two-step charge curve including a sloping region in the voltage range of 3.0-4.2 V and a flat plateau above 4.2 V. Furthermore, NLNM delivers a higher average voltage of ~3.4 V (vs ~2.4 V for NLM) and a lower overpotential of 35 mV at the 5th cycle (vs 91 mV for NLM), accompanied by significantly reduced voltage hysteresis in the first cycle compared to NLM. The capacity in the plateau above 3.8 V is generally attributed to the O-redox reaction[13]. In NLNM, the average oxidation state of Mn is close to +4, which limits further oxidize of Mn within the operating voltage window

In Press Accepted

Nano Research Energy
ISSN 2791-0091 (print); 2790-8119 (online)
https://doi.org/10.26599/NRE.2026.9120294

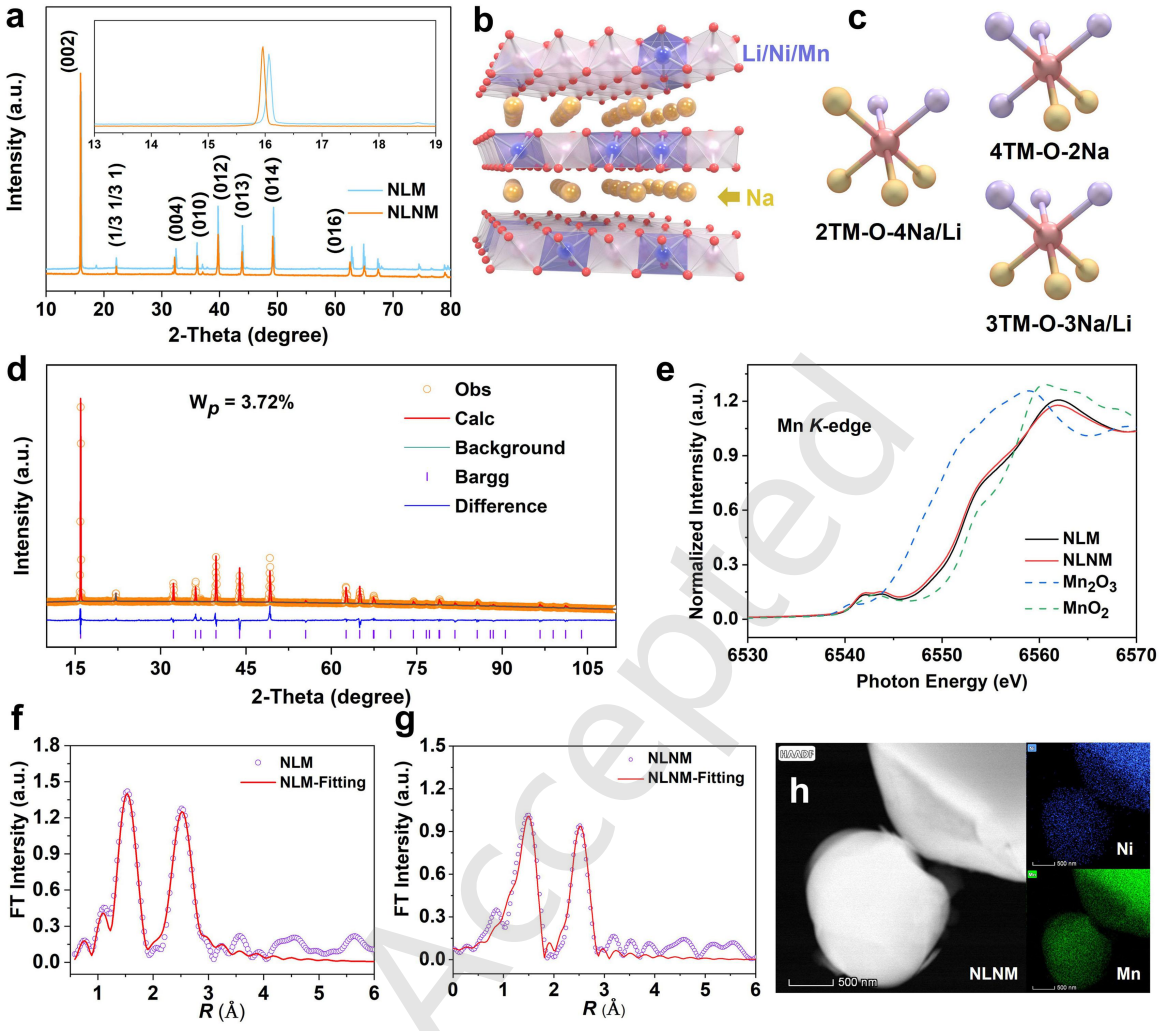


Figure 2 (a) XRD patterns of NLM and NLNM. Inset: enlarged view of (002) diffraction peaks. (b) Structural illustration of NLNM. (c) Local atomic coordination of oxygen-centered octahedron. (d) Rietveld refinements of the XRD pattern for NLNM. (e) XANES spectrum of Mn K-edge. The Mn K-edge EXAFS spectra and the corresponding fitting results of (f) NLM and (g) NLNM. (h) HAADF-STEM and mapping images of NLNM.

and consequently shifts the charge compensation to Ni redox (from Ni^{2+} to Ni^{4+}) in the lower-voltage region and oxygen redox (from O^{2-} to $(O_2)^{n-}$) at higher potentials[29]. The dQ/dV curve of NLNM (Figure S3) exhibits two oxidation peaks in the ranges of 2.8-3.5 V and 3.9-4.5 V, corresponding to Ni^{2+}/Ni^{4+} and $O^{2-}/(O_2)^{n-}$ redox pairs, respectively. During discharge, three reduction peaks appear at 3.7-4.1 V, 2.8-3.3 V, and in the low-voltage region (<2.5 V), corresponding to $(O_2)^{n-}$/ O^{2-}, Ni^{4+}/Ni^{2+}, and Mn^{4+}/Mn^{3+} redox pairs, respectively. The contribution of O-redox to the total capacity in NLNM is reduced compared with NLM, which can be attributed to the reduction of Na-O-Li configurations after Ni incorporation. These results demonstrate that Ni incorporation modulates the Ni/O redox chemistry and suppresses voltage hysteresis, thereby enabling improved electrochemical reversibility and overall performance in NLNM.

As shown in Figure 3c, the cell with NLNM delivers the high initial discharge capacity of about 151 mAh/g at 30 mA/g. Compared with the previously reported layered Mn-based oxide cathodes[9, 13, 29-35] (Figure S4), NLNM demonstrates competitive average voltage and discharge capacity. The kinetics of anionic redox were investigated by the galvanostatic intermittent titration technology (GITT) and the rate capability measurements. As shown in Figure S5, NLNM exhibits a smaller overpotential, especially in the high voltages region associated with oxygen redox reactions, indicating its excellent reaction kinetics and potential rate capability. The rate performance in Figure 3d and S6 further demonstrate the superior kinetics of NLNM, which delivers high discharge capacity of 132, 121, 111, 97, 87, 77, and 69 mAh/g from 50 to 1000 mA/g, respectively. When the current density returns to 100 mA/g, the capacity of NLNM recovers to its initial value and remains stable over subsequent cycles, demonstrating excellent reversibility at high rates. In contrast, the capacity of NLM declines to 70 mAh/g at 200

Just Accepted

Nano Research Energy
ISSN 2791-0091 (print); 2790-8119 (online)
https://doi.org/10.26599/NRE.2026.9120294

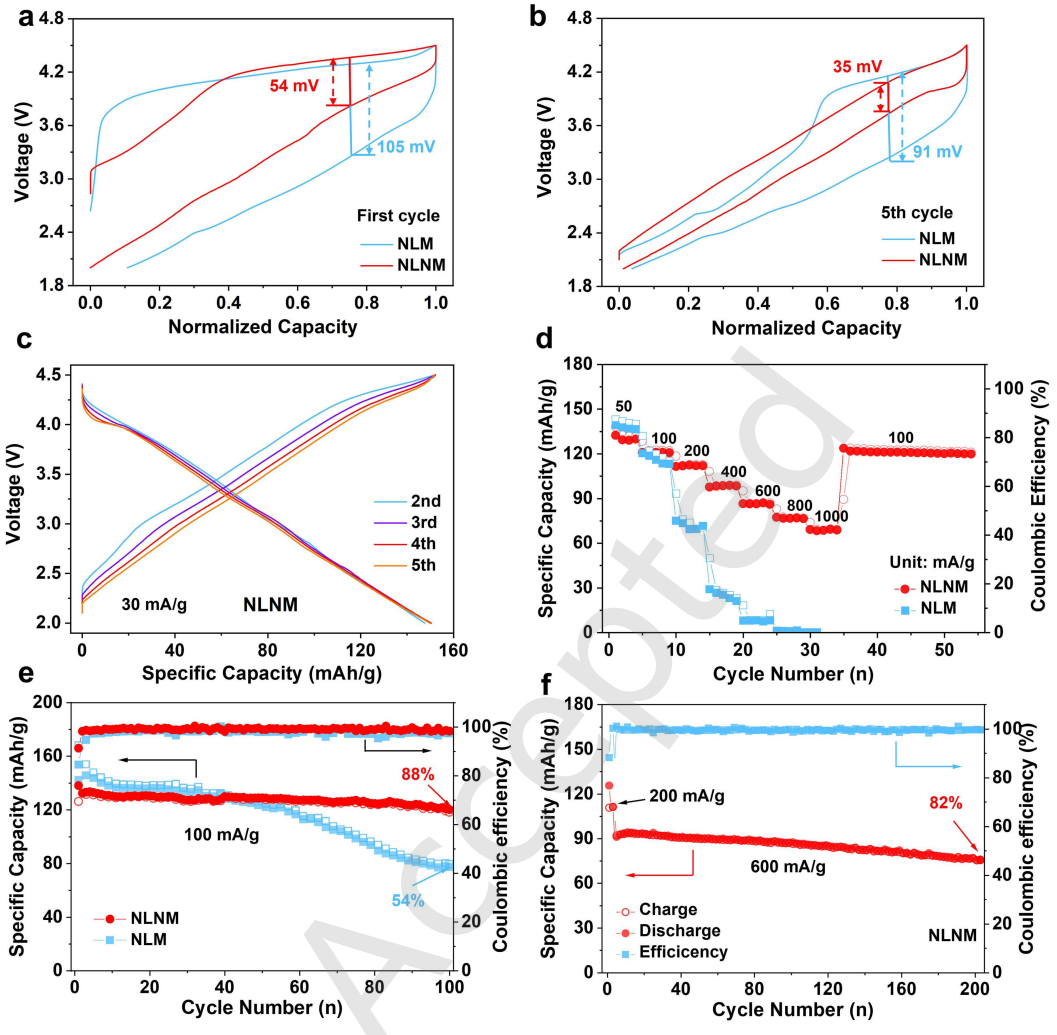


Figure 3 Normalized initial charge/discharge profiles of NLM and NLNM at different cycle: (a) 1st and (b) 5th. (c) The charge/discharge profiles of the initial cycles of NLNM at 30 mA/g. (d) Rate capability of NLM and NLNM. Cycling performance of NLM and NLNM with corresponding CE at different current densities: (e) 100 mA/g and (f) 600 mA/g.

mA/g and nearly 0 mAh/g at 600 mA/g, indicating the poor rate capability. The cycling performance of NLNM was further evaluated at 100 mA/g, as shown in Figure 3e. It delivers the reversible capacity of ~130 mAh/g with 88% capacity retention after 100 cycles, while NLM exhibits inferior cycling stability with only 54% retention. At higher current densities (Figure 3f and Figure S7), NLNM still deliver a high discharge capacity of ~92 mAh/g with stable Coulombic efficiency (CE), maintaining 82% capacity after 200 cycles. For comparison, NLM exhibits a much lower discharge capacity and retains only 62.9% of its initial capacity after 200 cycles at same condition (Figure S8), further highlighting the enhanced high-rate cycling stability of NLNM. These results indicate that the improved rate performance of NLNM is closely associated with the Ni-regulated charge compensation, which lowers the Na^+ migration barrier and promotes fast ion transport.

2.3 Charge Compensation and Structural Evolution

To explore the reversibility of oxygen redox and anionic activation at high current densities, we employed the soft X-ray absorption spectroscopy (SXAS) spectra with the total fluorescence yield (TFY) mode of the effective instrument for examining the oxidized oxygen species upon charging/discharging[11, 19]. Figure 4a exhibits the O K-edge SXAS spectra of NLNM at various charge/discharge states in the first cycle. The dominant pre-edge region below 532 eV can be divided into two peaks at 528.7 and 530.8 eV, corresponding to unoccupied O 2p states resulting from O 2p and TM 3d hybridization[36, 37] and O 2p - O 2p covalent interactions associated with oxidized oxygen species, respectively[19]. In case of O2p - TM 3d covalent mixing, the spectral weight of the pre-edge peak increases and shifts to lower energy with an increase in the valence state of 3d elements[38, 39]. Therefore, the intensity change of these peaks during charging/discharging reflects the changes in TM–O covalency and the formation of oxygen holes[40, 41]. Upon charging to 4.5 V, the apparent increase in shoulder peak intensity at ~530.8 eV can be

Just Accepted

Nano Research Energy

ISSN 2791-0091 (print); 2790-8119 (online)
https://doi.org/10.26599/NRE.2026.9120294

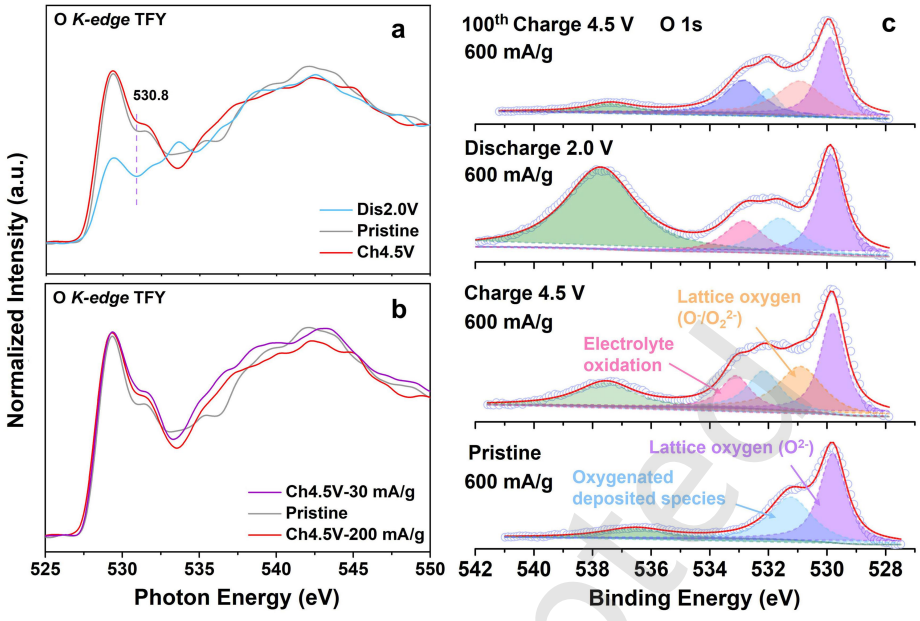


Figure 4 (a) The O-K edge SXAS spectra of NLNM at various charge/discharge states in the first cycle. (b) The O-K edge SXAS spectra of NLNM in the charged state at different current densities. (c) High-resolution O 1s XPS spectra of NLNM at various charge/discharge states at 600 mA/g.

observed compared with the pristine state, which is associated with the formation of O_2 at high charging state in $Na_x[Li_{0.25}Mn_{0.75}]O_2$[19]. When discharged to 2.0 V, the vanished peak at ~530.8 eV and the decreased intensity of the ~528.7 eV peak point to the refilling of the oxygen hole state and the reduction in the valence of Mn ion, respectively[42]. To further evaluate whether such oxygen redox is accompanied by irreversible oxygen loss, the lattice oxygen loss behavior of NLNM was also investigated by in-situ differential electrochemical mass spectrometry (DEMS), as plotted in Figure S9. O_2 signal cannot be detected during the entire charging process, indicating that suppressed irreversible lattice oxygen release. The DEMS result shows an extraordinary comparison to the one observed in the reported similar Na-oxygen cathode materials[32, 43], demonstrating that the increased TM-O covalency introduced by Ni incorporation plays a significant role in stabilizing lattice oxygen. The Ni redox reaction was highly reversible in NLNM electrode (Figure S10). The XANES spectra of NLNM shift to high photon energy after charging to 4.5 V (higher than that of $LiNi_{0.8}Mn_{0.1}Co_{0.1}O_2$ (NCM811)28), suggesting the oxidation of Ni^{2+} to Ni^{4+}. Upon discharge to 2.0 V, the oxidized Ni^{4+} was reduced to the initial Ni^{2+}, indicating the reversibility of Ni redox reaction in NLNM.

To investigate the oxygen redox activity when cycled at the high current density, O K-edge spectra of charged NLNM at 4.5 V were collected, as shown in Figure 4b. The peak intensity at 530.8 eV is significantly enhanced compared with the original state, implying the high activation of lattice oxygen upon charging. Given the considerable cycling stability of NLNM at 600 mA/g, the oxidation behavior of oxygen under high current density was further investigated. XPS was employed to examined the oxygen species of NLNM at different states in the first cycle and at the charge state of 4.5 V in the 100th cycle, as shown in Figure 4c. There are two types of lattice oxygen environments, including classical lattice O^{2-} at a binding energy of ~529.5 eV and the oxidized lattice oxygen $(O_2)^{n-}$ ($n<2$) at ~530.7 eV[18, 44]. A new peak at ~530.7 eV appears at the end of the charge state, suggesting the oxidation of lattice oxygen with the formation of peroxo-related species $(O_2)^{n-}$ [45, 46]. These results indicate the high activity of lattice oxygen even at a high current density of 600 mA/g. The disappearance of this peak at the end of discharge further confirms the high reversible activity of the peroxo-related species $(O_2)^{n-}$. After 100 cycles, the peak at 530.7 eV in O 1s XPS spectra under a charge state of 4.5 V can be clearly observed, demonstrating that lattice oxygen can participate in charge compensation and keep high reversibility in the long-term cycles even at high current density.

The in-situ XRD technique was employed to monitor the variation of lattice parameters and the structural evolution of NLNM during Na+ de/intercalation, as shown in Figure 5a. The in-situ XRD patterns collected over the initial cycle exhibit a single P2 phase with all diffraction peaks shifting continuously during the charge/discharge (Figure 5b), demonstrating its excellent structure reversibility. The (002) peak shifts to lower 2 , while the (100) peaks shifts to higher 2 during charging, indicates that the increase in *c*-axis and the decrease in the *a*-axis

Just Accepted

Nano Research Energy
ISSN 2791-0091 (print); 2790-8119 (online)
https://doi.org/10.26599/NRE.2026.9120294

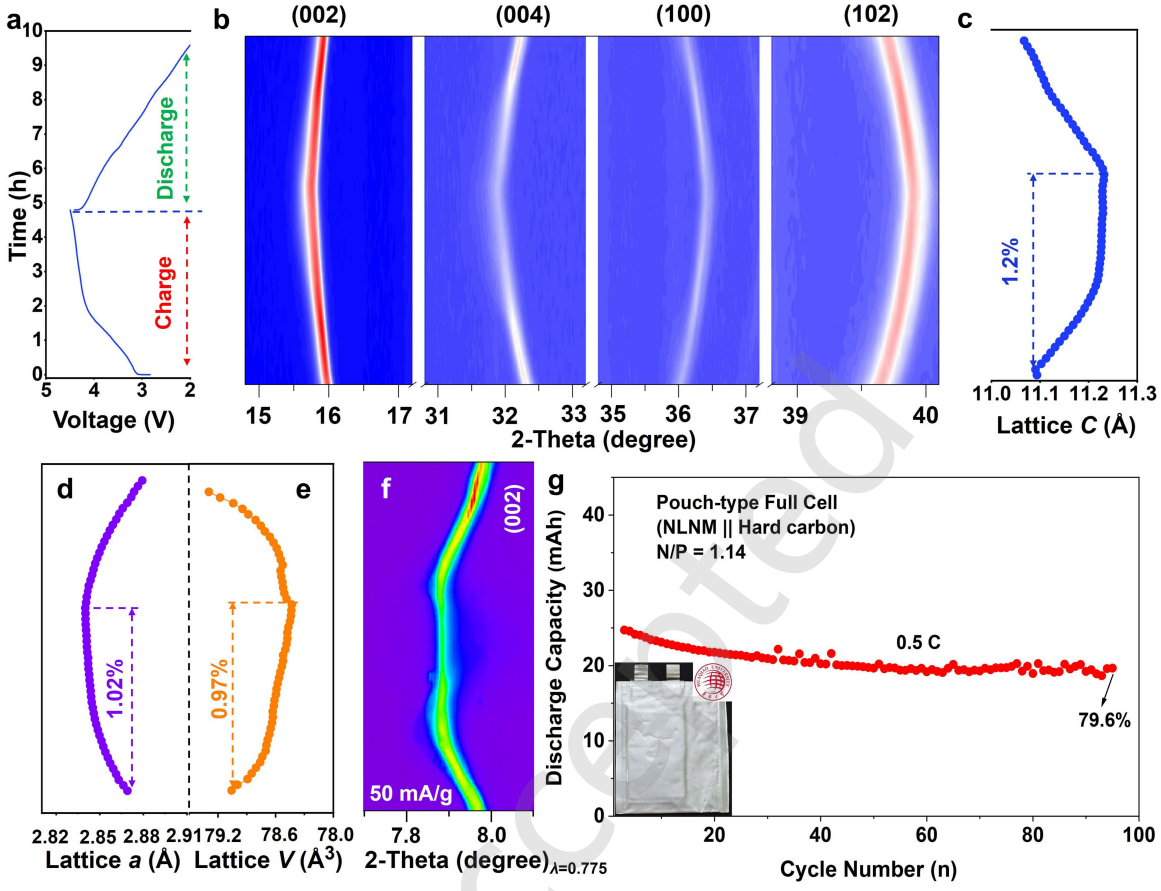


Figure 5 (a) The typical first charge/discharge profile of NLNM. (b) In-situ XRD patterns of NLNM collected at a current density of 15 mA/g. The evolution of parameter lattice (c) c, (d) a and (e) V. (f) Contour plot of the (002) peak evolutions of NLNM in the first cycle at 50 mA/g. (g) The cycling performance of Pouch-type full cell of NLNM||HC.

lattice parameters. Structural degradation of P2-type layered oxides at high states of charge is generally associated with pronounced lattice distortion and stacking transitions, and suppressing such structural reconstruction has been demonstrated to be critical for achieving highly reversible Na storage[47, 48]. The evolution of the lattice parameters derived from the XRD patterns is displayed in Figure 5c-e. The evolution of the calculated c-axis is only 1.2%, which is much lower than those of the previous works[9, 13] (Figure 5c). Furthermore, the *a*-axis gradually decreases during charging, which is associated with the oxidation of Ni and oxygen, leading to enhanced TM-O covalency and strengthened in plane bonding (Figure 5d). The expansion of the *c*- axis arises from the increased electrostatic repulsion between adjacent oxygen layers as Na ions are extracted from the structure, thereby weakening the screening effect and forcing the layers apart. The combination of a-axis contraction and c-axis expansion results in a remarkably small unit-cell volume variation of only 0.97% during cycling (Figure 5e). Such highly reversible lattice evolution indicates that NLNM effectively accommodates the structural strain generated during Na extraction and insertion. However, the small c-axis and volume variations do not directly quantify TMO_2 slab sliding, which primarily involves a lateral shear displacement of adjacent slabs. Rather, these lattice parameters represent the macroscopic response of the average P2 framework. Together with the continuous evolution of the diffraction peaks without a detectable long-range stacking transition, these results demonstrate the high structural reversibility of NLNM during deep desodiation. As discussed below, we attribute this behavior partly to the adaptive Ni-regulated local bonding network, which accommodates local distortion and increases the resistance against cooperative slab rearrangement. To further evaluate the structure evolution at high current density, in-situ synchrotron XRD technique (wavelength = 0.775) was performed at 50 mA/g. In order to obtain high-quality data during the fast charge/discharge, XRD patterns were collected within a narrow 2 angle range of around (002) peak. As shown in Figure 5f, the (002) peak continuously shifts during the first cycle, indicating a solid-solution reaction within a single P2 phase, consistent with the results in Figure 5b. To evaluate the practical prospects of NLNM, pouch-type full cell of NLNM||HC was assembled. As shown in Figure 5g and S10, prior to cycling tests, the pouch cell

Just Accepted

Nano Research Energy
ISSN 2791-0091 (print); 2790-8119 (online)
https://doi.org/10.26599/NRE.2026.9120294

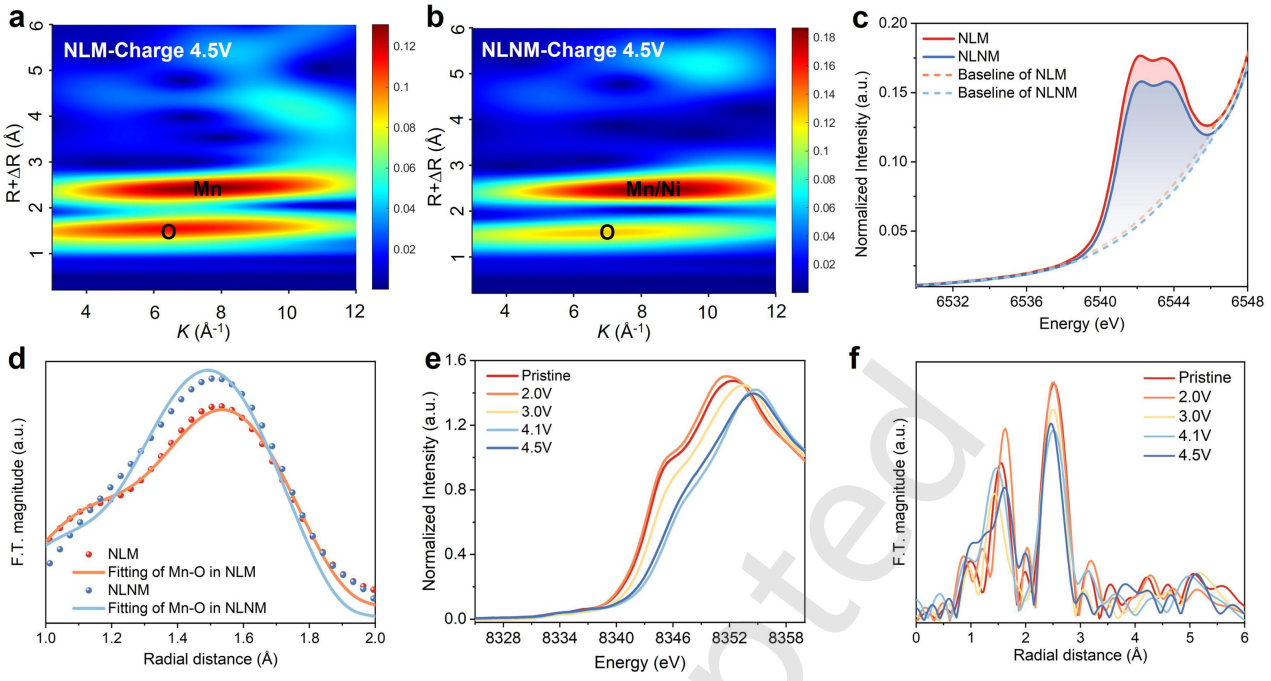


Figure 6 Wavelet transforms of the k^3-weighted EXAFS for (a) the NLM and (b) the NLNM samples, highlighting the distribution of backscattering atoms in both *k*- and *R*-space. (c) A magnified view of the pre-edge region of the normalized XANES spectra. (d) Fourier transform and the corresponding shell fitting results for the Mn K-edge EXAFS. (e) Ex-situ Ni K-edge XANES spectra and (f) the corresponding Fourier transforms of the EXAFS for the NLNM sample collected at pristine and different voltage state.

underwent two pre-cycles at a rate of 0.2 C, during which the irreversible capacity loss was primarily attributed to insufficient coulombic efficiency in both the cathode and anode. The cell can deliver a reversible capacity of ~38.5 mAh and a high average working voltage of about 3.6 V within a voltage range of 1.5-4.4 V. Moreover, the cell exhibits good cycling stability, with capacity retention of 79.6% after nearly 100 cycles at 0.5 C.

To elucidate the mechanism underlying the electrochemical behavior of NLNM upon Ni incorporation, ex-situ EXAFS analysis was conducted to probe the redox chemistry of Mn and Ni at their respective K-edges. As shown in Figure 6a,b, wavelet transforms of the Mn EXAFS signals for NLM and NLNM are reveal the scattering contributions of backscattering atoms in both *k*- and *R*-space. Upon Ni incorporation, the integrated area of the Mn pre-edge feature decreases by approximately 17% relative to pristine NLM (Figure 6c), indicating a modification in the local coordination symmetry around Mn ions. Quantitative finding demonstrates that Ni doping mitigates the symmetry-breaking Jahn–Teller effect of Mn^{3+} through the strong oxidizing nature of Ni^{4+}, thereby lowering the fraction of Jahn–Teller-active Mn^{3+} in the lattice.

Parallel ex-situ Ni K-edge XANES and EXAFS analyses were performed to track the evolution of the local Ni coordination during cycling (Figure 6e,f). With increasing voltage, the Ni absorption edge progressively shifts toward higher energy, confirming the oxidation of Ni^{2+} /Ni^{3+} toward Ni^{4+}. The Ni–O distance initially decreases upon charging to 4.1 V, consistent with the progressive oxidation of Ni, whereas a reversed variation is observed upon further charging to 4.5 V as oxygen redox becomes increasingly involved. Therefore, the non-monotonic Ni–O evolution should not be regarded as a simple mechanical contraction and expansion of an isolated Ni–O bond. Instead, it reflects an adaptive reorganization of the Ni-centered coordination environment in response to the coupled Ni/O redox chemistry and the strongly perturbed oxygen framework at deep desodiation. On this basis, we define the structural "spring effect" as the reversible local distortion and relaxation of the Ni-regulated TM–O bonding network rather than a uniaxial spring operating along the c-axis. Although this collective sliding coordinate is geometrically distinct from the local Ni–O bond length variation, the two are coupled through the shared oxygen framework. The adaptive Ni-centered coordination can accommodate local deformation generated during Na extraction, while the strengthened metal–oxygen bonding network provides an energetic restoring tendency against irreversible oxygen framework rearrangement. Such a local bonding response can therefore increase the resistance to cooperative slab gliding and prevent local structural perturbations from developing into a long-range stacking transformation. We refer to this coupled local-bonding response as the Ni-induced structural "spring effect".

Just Accepted

Nano Research Energy
ISSN 2791-0091 (print); 2790-8119 (online)
https://doi.org/10.26599/NRE.2026.9120294

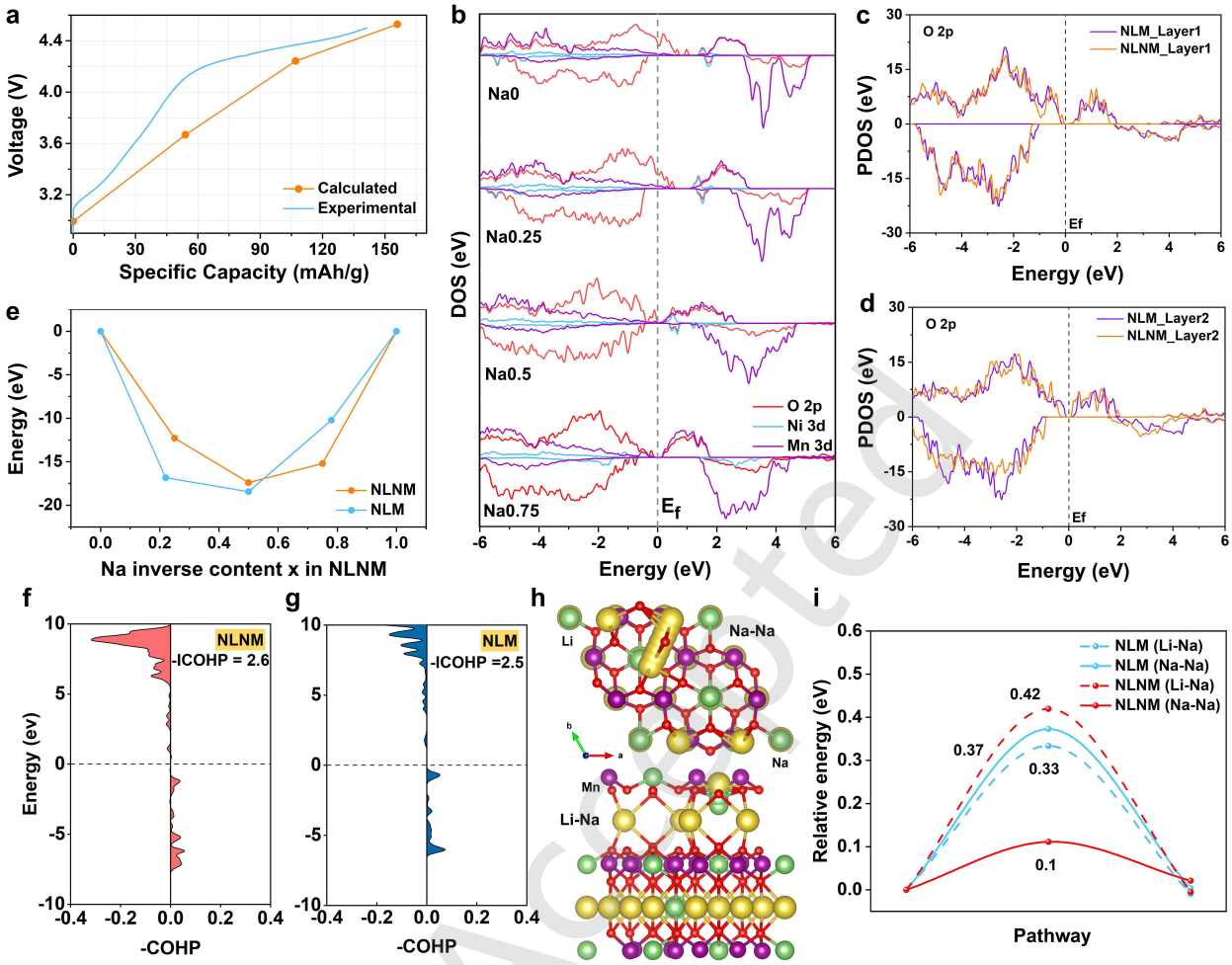


Figure 7 (a) A combined graph of the galvanostatic charge profile of NLNM to 4.5 V with a theoretically calculated charge profile. (b) Projected DOS of the O 2p, Mn 3d, and Ni 3d orbitals of NLNM with different Na content. O 2p PDOS at different layers in the NLM and NLNM of (c) layer1 and (d) layer2. (e) Formation energies of mixing enthalpy of NLM and NLNM at various desodiated states. ICOHP values of the bond between lithium and the surrounding six oxygen atoms of (f) NLM and (g) NLNM. (h) Schematic illustration of crystal structure for Na ion migration of Na to Na in the intra-layer and Li to Na in the inter-layer. (i) The corresponding migration energy of Na ions and Li ions in NLM and NLNM.

2.4 DFT Calculation and Simulations

Figure 7a demonstrates the galvanostatic charge curve of NLNM and the theoretically calculated voltage profile. The calculated charge voltage curve shows a two-step charging with one sloppy region in a voltage range from 3.0 to 4.2 V and the flat plateau above 4.2 V, which is well in agreement with the experimental results (blue line). To clarify the charge compensation mechanism in NLNM during desodiation, the electronic structures of Mn, Ni, and O were analyzed by density functional theory (DFT) calculations, as shown in Figure 7b. The deviation between the simulated formula and the actual stoichiometry of the material is attributed to the limitations of the unit cell model, which is a common phenomenon in layered oxide cathode calculations and does not affect the validity of the results[49, 50]. The electron densities at the Ni 3d orbitals around the Fermi level (EF) decreased upon Na extraction from 0.75 to 0.5, revealing that Ni redox dominated the charge compensation in this charge process. With further Na extraction from 0.5 to 0.25, the electron-hole densities of O 2p orbitals above EF are generated suggesting that the lattice oxygen starts to participate in charge compensation. Subsequently, the electron hole densities of the O 2p orbitals further increased upon full desodiation, implying the continuous capacity contribution from the redox reaction of oxygen. These results demonstrate that O2-/1- redox reactions occur in NLNM, consistent with the findings of previous works[21, 35]. To further elucidate the role of Ni doping in NLMN, the O 2p Partial Density of States (PDOS) was analyzed Ni-free and Ni-containing system (Figure S11). As shown in Figure 7c and S12, neither NLM nor NLNM has Ni doping in Layer1, and the O 2p orbitals have approximately the same density of states. However, NLNM has Ni doping in Layer 2 (Figure 7d),

Just Accepted

which can be seen as a significant downward shift of the top of the valence band of the O 2p orbital, reducing its ability to give electrons. This enhances the chemical stability of the TM coordination oxygen ion and suppresses the oxygen liberation.

To evaluate the effect of Ni incorporation on the thermodynamic stability of NLM during desodiation, the mixing enthalpy at various Na concentrations in NLM and NLNM (Figure 7e). At Na content above 0.5, both NLM and NNM exhibit relatively low mixing enthalpies, indicating the stable sodium-deficient phases. However, the mixing enthalpy values of NLM and NLNM increase with further desodiation, which indicates a decrease in the relative phase stability of both NLM and NNLM. This change in thermodynamic phase stability at high Na desodiation process is associated with the anion-based redox reaction of O^{2-}/O^{n-} [34]. Notably, NLNM exhibits a smaller slope in the mixing enthalpy curve in the range of 0.5-0.76 compared with NLM, implying that Ni incorporation suppresses the formation of unstable phases and enhances structural stability during deep desodiation.

To further understand the bonding origin of this adaptive structural response, crystal orbital Hamiltonian population (COHP) analysis was performed for NLM and NLNM (Figure 7f,g). The integrated −COHP value of the Li–O interaction increases from 2.5 to 2.6 upon Ni incorporation, indicating strengthened local bonding within the TM–O framework. ELF analysis further reveals a redistribution of electron density around oxygen after Ni incorporation (Figure S13), supporting the modification of the local metal–oxygen bonding environment. Because lateral TMO_2 slab gliding necessarily requires coordinated displacement and rearrangement of the shared oxygen framework, strengthening these local interactions is expected to increase the energetic penalty associated with collective slab displacement. Therefore, the Ni-regulated bonding network provides a microscopic basis for the enhanced resistance against cooperative layer gliding, connecting the local structural “spring” response with the macroscopic stability of the P2 framework.

To understand the superior rate performance of NLNM, the Na^+ and Li+ diffusion pathway and migration barriers were evaluated (Figure 7h). Ni incorporation markedly reduces the Na^+ migration barrier from 0.37 eV in NLM to 0.1 eV in NLNM, facilitating rapid ion diffusion and enhanced rate capability. In Mn-based oxide cathodes with high anodic redox activity, Li^+ migration from TM layers to Na layers during charging can induce structural degradation and poor cycling stability. The migration barrier for Li+ increases from 0.33 eV in NLM to 0.42 eV in NLNM, indicating that Ni doping effectively suppresses Li+ migration and improves structural integrity.

3 Conclusions

In summary, we have successfully demonstrated a P2-type NLNM cathode by partially substituting Li with electrochemically active Ni, which introduces a pronounced Ni-induced structural “spring effect”. The results reveal that the enhanced Ni-O covalency plays a multifaceted role in performance optimization: (i) it stabilizes anionic redox by accelerating oxygen redox kinetics and mitigating irreversible oxygen loss; (ii) it functions as a structural "spring" that mitigates the volume variation of the unit cell during Na^+ extraction and insertion, suppressing detrimental phase transitions at deep desodiation states; and (iii) it alleviates the Jahn–Teller distortion of Mn^{3+} by modulating the local coordination environment, minimizing anisotropic lattice strain. These synergistic effects collectively enable NLNM to deliver a high reversible capacity of ~150 mAh/g at an average voltage of 3.4 V, along with robust rate capability and cycling stability, maintaining 82% capacity retention after 200 cycles at 600 mA/g. This work demonstrates a structure-designed strategy for improving specific energy and stability of electrodes for high performance SIBs.

Acknowledgements

This work was supported by the National Natural Science Foundation of China (52502254), the Significant Science and Technology Project in Xiamen (Future Industry field) (3502Z20241033) and Huaqiao University Research Startup Funds (605-50Y25014). We also acknowledge the support from the Max Planck POSTECH-Hsinchu Center for Complex Phase Materials. The part of the research work described in this paper was conducted in the JC STEM Lab of Energy and Materials Physics funded by The Hong Kong Jockey Club Charities Trust.

Electronic Supplementary Material: Supplementary material (materials synthesis, materials characterization, calculation methods, Figures S1-S13, Tables S1-S5) is available in the online version of this article at https://doi.org/10.26599/NRE.2026.9120294.

References

[1] Shi, S.; Yang, Q.; Sui, S.; Li, S.; Li, L.; Lei, K.; Zheng, S. Boosting the Sodium Storage Performance of O3-Type Layered Oxide Cathode by Dual-Site Doping. Nano Lett. 2025, 25, 10034–10043.

[2] Usiskin, R.;Lu, Y.;Popovic, J.;Law, M.;Balaya, P.;Hu, Y.-S.; Maier, J. Fundamentals, status and promise of sodium-based batteries. Nat. Revi. Mater. 2021, 6, 1020-1035.

[3] Zhang, T.; Song, Z.; Li, Y.; Huang, Y.; Su, J.; Hua, W.; Li, F. Intergrowth of Prismatic and Octahedral Layers to Inhibit Fe Migration in Oxide Cathodes for Sodium-Ion Batteries. Angew. Chem. Int. Ed. 2025, 64, e202509816.

[4] Liu, Q.;Li, Y.;Su, Y.;Fan, Y.;Hu, F.;Li, C.;Tian, L.;Luo, Y.;Cao, B.;Xu, L.;Meng, Q.; Dong, P. Challenges and strategic approaches to constructing the full life cycle value chain of layered cathode materials for sodium-ion batteries. Nano Research Energy 2026, 5.

[5] Liu, Q.;Hu, Z.;Li, W.;Zou, C.;Jin, H.;Wang, S.;Chou, S.; Dou, S.-X. Sodium transition metal oxides: the preferred cathode choice for future sodium-ion batteries? Energy Environ. Sci. 2021, 14, 158-179.

[6] Huo, T.; Yang, Q.; Yu, G.; Li, M.; Bai, X.; Lv, T.; Li, L.; Lei, K.; Zheng, S. Regulation of local chemistry in O3-type layered oxide cathodes for practical sodium-ion batteries Chem. Sci. 2026, 17, 11643–11654.

[7] Park, J.-H.;Ko, I.-H.;Lee, J.;Park, S.;Kim, D.;Yu, S.-H.; Sung, Y.-E. Anionic Redox Reactions in Cathodes for Sodium-Ion Batteries.

Just Accepted

ChemElectroChem 2021, 8, 625-643.

[8] Rahman, M. M.; Lin, F. Oxygen Redox Chemistry in Rechargeable Li-Ion and Na-Ion Batteries. Matter 2021, 4, 490-527.

[9] Yabuuchi, N.;Hara, R.;Kajiyama, M.;Kubota, K.;Ishigaki, T.;Hoshikawa, A.; Komaba, S. New O2/P2-type Li-Excess Layered Manganese Oxides as Promising Multi-Functional Electrode Materials for Rechargeable Li/Na Batteries. Adv. Energy Mater. 2014, 4, 201301453.

[10] Maitra, U.;House, R. A.;Somerville, J. W.;Tapia-Ruiz, N.;Lozano, J. G.;Guerrini, N.;Hao, R.;Luo, K.;Jin, L.;Perez-Osorio, M. A.;Massel, F.;Pickup, D. M.;Ramos, S.;Lu, X.;McNally, D. E.;Chadwick, A. V.;Giustino, F.;Schmitt, T.;Duda, L. C.;Roberts, M. R.; Bruce, P. G. Oxygen redox chemistry without excess alkali-metal ions in Na2/3[Mg0.28Mn0.72]O2. Nat. Chem. 2018, 10, 288-295.

[11] Wang, Q.;Liao, Y.;Jin, X.;Cheng, C.;Chu, S.;Sheng, C.;Zhang, L.;Hu, B.;Guo, S.; Zhou, H. Dual Honeycomb-Superlattice Enables Double-High Activity and Reversibility of Anion Redox for Sodium-Ion Battery Layered Cathodes. Angew. Chem. Int. Ed. 2022, 61, e202206625.

[12] Zhanadilov, O.;Baiju, S.;Voronina, N.;Yu, J. H.;Kim, A. Y.;Jung, H. G.;Ihm, K.;Guillon, O.;Kaghazchi, P.; Myung, S. T. Impact of Transition Metal Layer Vacancy on the Structure and Performance of P2 Type Layered Sodium Cathode Material. Nanomicro Lett. 2024, 16, 239.

[13] Rong, X.;Hu, E.;Lu, Y.;Meng, F.;Zhao, C.;Wang, X.;Zhang, Q.;Yu, X.;Gu, L.;Hu, Y.-S.;Li, H.;Huang, X.;Yang, X.-Q.;Delmas, C.; Chen, L. Anionic Redox Reaction-Induced High-Capacity and Low-Strain Cathode with Suppressed Phase Transition. Joule 2019, 3, 503-517.

[14] Liu, T.;Tan, H.;Wang, J.;Li, C.;Liu, Z.;Wu, Z.;Hu, Y.; Peng, S. Activating Reversible Anionic Redox in Layered Oxide Cathodes for Highly Stable Sodium-Ion Batteries by Li/Nb Codoping. ACS Nano 2026, 20, 14145-14154.

[15] Wang, X.; Zhang, Q.; Zhao, C. Li, H.; Zhang, B.; Zeng, G.; Tang, Y.; Huang, Z.; Hwang, I.; Sun, Y.; Wang, Q.; Xu, G.; Gu, L.; Qiao, Y.; Sun, S. Achieving a high-performance sodium-ion pouch cell by regulating intergrowth structures in a layered oxide cathode with anionic redox. Nat. Energy 2024,9, 184–196.

[16] Hu, C.;Lou, X.;Liu, J.;Li, J.;Tong, W.;Li, H.;Zou, Y.;Hu, B.; Li, C. Accumulation of Unreduced Molecular O2 Explains Abnormal Voltage Decay in P2 - Type Layered Oxide Cathode. Adv. Energy Mater. 2025, 15, e03491.

[17] Rahman, M. M.;McGuigan, S.;Li, S.;Gao, L.;Hou, D.;Yang, Z.;Xu, Z.;Lee, S.-J.;Sun, C.-J.;Liu, J.;Huang, X.;Xiao, X.;Chu, Y.;Sainio, S.;Nordlund, D.;Kong, X.;Liu, Y.; Lin, F. Chemical Modulation of Local Transition Metal Environment Enables Reversible Oxygen Redox in Mn-Based Layered Cathodes. ACS Energy Lett. 2021, 6, 2882-2890.

[18] Wang, Q.;Mariyappan, S.;Rousse, G.;Morozov, A. V.;Porcheron, B.;Dedryvère, R.;Wu, J.;Yang, W.;Zhang, L.;Chakir, M.;Avdeev, M.;Deschamps, M.;Yu, Y.-S.;Cabana, J.;Doublet, M.-L.;Abakumov, A. M.; Tarascon, J.-M. Unlocking anionic redox activity in O3-type sodium 3d layered oxides via Li substitution. Nat. Mater. 2021, 20, 353-361.

[19] House, R. A.;Maitra, U.;Pérez-Osorio, M. A.;Lozano, J. G.;Jin, L.;Somerville, J. W.;Duda, L. C.;Nag, A.;Walters, A.;Zhou, K.-J.;Roberts, M. R.; Bruce, P. G. Superstructure control of first-cycle voltage hysteresis in oxygen-redox cathodes. Nature 2020, 577, 502-508.

[20] Li, Y.;Wang, X.;Gao, Y.;Zhang, Q.;Tan, G.;Kong, Q.;Bak, S.;Lu, G.;Yang, X.-Q.;Gu, L.;Lu, J.;Amine, K.;Wang, Z.; Chen, L. Native Vacancy Enhanced Oxygen Redox Reversibility and Structural Robustness. Adv. Energy Mater. 2018, 9, 201803087.

[21] Kim, D.;Cho, M.; Cho, K. Rational Design of Na(Li1/3Mn2/3)O2 Operated by Anionic Redox Reactions for Advanced Sodium-Ion Batteries. Adv. Mater. 2017, 29, 201701788.

[22] Cho, M. J.;Yaqoob, N.;Yu, J. H.;Köster, K.;Kim, A. Y.;Jung, H. G.;Ihm, K.;Lee, K. S.;Avdeev, M.;Kim, H.;Kaghazchi, P.; Myung, S. T. Theoretical and Experimental Optimization of P2 - Type Sodium - Ion Battery Cathodes via Li, Mg, and Ni Co - Doping: A Path to Enhanced Capacity and Stability. Adv. Energy Mater. 2024, 15, 202405112.

[23] Li, N.;Zhao, E.;Zhang, Z.;Yin, W.;He, L.;Wang, B.;Wang, F.;Xiao, X.; Zhao, J. Gradient and De - Clustered Anionic Redox Enabled Undetectable O2 Formation in 4.5 V Sodium Manganese Oxide Cathodes. Adv. Mater. 2024, 36, 202408984.

[24] Wang, X.;Yang, Z.;Cai, Y.;Ma, H.;Xu, J.;Khatoon, R.;Ye, Z.;Wang, D.;Sajjad, M. T.; Lu, J. Regulation Engineering of Alkali Metal Interlayer Pillar in P2-Type Cathode for Ultra-High Rate and Long-Term Cycling Sodium-Ion Batteries. Nanomicro Lett. 2026, 18, 105.

[25] Gao, A.;Zhang, Q.;Li, X.;Shang, T.;Tang, Z.;Lu, X.;Luo, Y.;Ding, J.;Kan, W. H.;Chen, H.;Yin, W.;Wang, X.;Xiao, D.;Su, D.;Li, H.;Rong, X.;Yu, X.;Yu, Q.;Meng, F.;Nan, C.;Delmas, C.;Chen, L.;Hu, Y.-S.; Gu, L. Topologically protected o0x36ygen redox in a layered manganese oxide cathode for sustainable batteries. Nat. Sustain. 2022, 5, 214-224.

[26] Abate, I.;Kim, S. Y.;Pemmaraju, C. D.;Toney, M. F.;Yang, W.;Devereaux, T. P.;Chueh, W. C.; Nazar, L. F. The Role of Metal Substitution in Tuning Anion Redox in Sodium Metal Layered Oxides Revealed by X-Ray Spectroscopy and Theory. Angew. Chem. Int. Ed. 2021, 60, 2 – 10.

[27] Jin, W.;Myeong, S.;Hwang, J.;Jang, H.;Sung, J.;Yoo, Y.;Kim, M. G.; Cho, J. Unraveling the Rapid Redox Behavior of Li-Excess 3d-Transition Metal Oxides for High Rate Capability. Adv. Energy Mater. 2020, 10, 1904092.

[28] Huang, Y.;Zhu, Y.;Nie, A.;Fu, H.;Hu, Z.;Sun, X.;Haw, S.-C.;Chen, J.-M.;Chan, T.-S.;Yu, S.;Sun, G.;Jiang, G.;Han, J.;Luo, W.; Huang, Y. Enabling Anionic Redox Stability of P2-Na5/6Li1/4Mn3/4O2 by Mg Substitution. Adv. Mater. 2022, 34, 2105404.

[29] Voronina, N.;Shin, M.-Y.;Kim, H.-J.;Yaqoob, N.;Guillon, O.;Song, S. H.;Kim, H.;Lim, H.-D.;Jung, H.-G.;Kim, Y.;Lee, H.-K.;Lee, K.-S.;Yazawa, K.;Gotoh, K.;Kaghazchi, P.; Myung, S.-T. Hysteresis-Suppressed Reversible Oxygen-Redox Cathodes for Sodium-Ion Batteries. Adv. Energy Mater. 2022, 12, 2103939.

[30] Yang, L.;Kuo, L.-Y.;López del Amo, J. M.;Nayak, P. K.;Mazzio, K. A.;Maletti, S.;Mikhailova, D.;Giebeler, L.;Kaghazchi, P.;Rojo, T.; Adelhelm, P. Structural Aspects of P2-Type Na0.67Mn0.6Ni0.2Li0.2O2 (MNL) Stabilization by Lithium Defects as a Cathode Material for Sodium-Ion Batteries. Adv. Funct. Mater. 2021, 31, 2102939.

[31] Li, C.;Zhao, C.;Hu, B.;Tong, W.;Shen, M.; Hu, B. Unraveling the Critical Role of Ti Substitution in P2-NaxLiyMn1–yO2 Cathodes for Highly Reversible Oxygen Redox Chemistry. Chem. Mater. 2020, 32, 1054-1063.

[32] Cao, X.;Li, X.;Qiao, Y.;Jia, M.;Qiu, F.;He, Y.;He, P.; Zhou, H. Restraining Oxygen Loss and Suppressing Structural Distortion in a Newly Ti-Substituted Layered Oxide P2-Na0.66Li0.22Ti0.15Mn0.63O2. ACS Energy Lett. 2019, 4, 2409-2417.

[33] Zhang, K.;Kim, D.;Hu, Z.;Park, M.;Noh, G.;Yang, Y.;Zhang, J.;Lau, V. W.;Chou, S. L.;Cho, M.;Choi, S. Y.; Kang, Y. M. Manganese based layered oxides with modulated electronic and thermodynamic properties for sodium ion batteries. Nat. Commun. 2019, 10, 5203.

[34] Kang, S. M.;Kim, D.;Lee, K.-S.;Kim, M.-S.;Jin, A.;Park, J.-H.;Ahn, C.-Y.;Jeon, T.-Y.;Jung, Y. H.;Yu, S.-H.;Mun, J.; Sung, Y.-E. Structural and Thermodynamic Understandings in Mn-Based Sodium Layered Oxides during Anionic Redox. Adv. Sci. 2020, 7,

Just Accepted

2001263.

[35] Konarov, A.;Kim, H. J.;Jo, J.-H.;Voronina, N.;Lee, Y.;Bakenov, Z.;Kim, J.; Myung, S.-T. High-Voltage Oxygen-Redox-Based Cathode for Rechargeable Sodium-Ion Batteries. Adv. Energy Mater. 2020, 10, 2001111.

[36] Read, N.; Green, D. Paired states of fermions in two dimensions with breaking of parity and time-reversal symmetries and the fractional quantum Hall effect. Phys. Rev. B 2000, 61, 10267-10297.

[37] Tjeng, L. H.;Chen, C. T.; Cheong, S. W. Comparative soft-x-ray resonant-photoemission study on Bi2Sr2CaCu2O8, CuO, and Cu2O. Phys. Rev. B 1992, 45, 8205-8208.

[38] Guo, H.;Li, Z. W.;Zhao, L.;Hu, Z.;Chang, C. F.;Kuo, C. Y.;Schmidt, W.;Piovano, A.;Pi, T. W.;Sobolev, O.;Khomskii, D. I.;Tjeng, L. H.; Komarek, A. C. Antiferromagnetic correlations in the metallic strongly correlated transition metal oxide LaNiO3. Nat. Commun. 2018, 9, 43.

[39] Chin, Y. Y.;Hu, Z.;Lin, H. J.;Agrestini, S.;Weinen, J.;Martin, C.;Hébert, S.;Maignan, A.;Tanaka, A.;Cezar, J. C.;Brookes, N. B.;Liao, Y. F.;Tsuei, K. D.;Chen, C. T.;Khomskii, D. I.; Tjeng, L. H. Spin-orbit coupling and crystal-field distortions for a low-spin 3d5 state in BaCoO3. Phys. Rev. B 2019, 100, 205139.

[40] Abbate, M.;de Groot, F. M. F.;Fuggle, J. C.;Fujimori, A.;Strebel, O.;Lopez, F.;Domke, M.;Kaindl, G.;Sawatzky, G. A.;Takano, M.;Takeda, Y.;Eisaki, H.; Uchida, S. Controlled-valence properties of La1−xSrxFeO3 and La1−xSrxMnO3 studied by soft-x-ray absorption spectroscopy. Phys. Rev. B 1992, 46, 4511-4519.

[41] Chin, Y.-Y.;Hu, Z.;Shimakawa, Y.;Yang, J.;Long, Y.;Tanaka, A.;Tjeng, L. H.;Lin, H.-J.; Chen, C.-T. Charge and spin degrees of freedom in A-site ordered YCu3Co4O12 and CaCu3Co4O12. Phys. Rev. B 2021, 103, 115149.

[42] Yang, L.;Liu, Z.;Shen, X.;Li, S.;Hu, Z.;Kong, Q.;Ma, J.;Li, J.;Lin, H.-J.;Chen, C.-T.;Chen, J.-M.;Haw, S.-C.;Wang, X.;Yu, R.;Wang, Z.; Chen, L. Effect of vacancy-tailored Mn3+ spinning on enhancing structural stability. Energy Storage Mater. 2022, 44, 231-238.

[43] Zhao, C.;Yang, Q.;Geng, F.;Li, C.;Zhang, N.;Ma, J.;Tong, W.; Hu, B. Restraining Oxygen Loss and Boosting Reversible Oxygen Redox in a P2-Type Oxide Cathode by Trace Anion Substitution. ACS Appl. Mater. Interfaces 2021, 13, 360-369.

[44] Assat, G.;Iadecola, A.;Foix, D.;Dedryvère, R.; Tarascon, J.-M. Direct Quantification of Anionic Redox over Long Cycling of Li-Rich NMC via Hard X-ray Photoemission Spectroscopy. ACS Energy Lett. 2018, 3, 2721-2728.

[45] Pearce, P. E.;Perez, A. J.;Rousse, G.;Saubanère, M.;Batuk, D.;Foix, D.;McCalla, E.;Abakumov, A. M.;Van Tendeloo, G.;Doublet, M.-L.; Tarascon, J.-M. Evidence for anionic redox activity in a tridimensional-ordered Li-rich positive electrode β-Li2IrO3. Nat. Mater. 2017, 16, 580-586.

[46] Zhang, X.;Qiao, Y.;Guo, S.;Jiang, K.;Xu, S.;Xu, H.;Wang, P.;He, P.; Zhou, H. Manganese-Based Na-Rich Materials Boost Anionic Redox in High-Performance Layered Cathodes for Sodium-Ion Batteries. Adv. Mater. 2019, 31, 1807770.

[47] Tang, Y.;Zhang, Q.;Zuo, W.;Zhou, S.;Zeng, G.;Zhang, B.;Zhang, H.;Huang, Z.;Zheng, L.;Xu, J.;Yin, W.;Qiu, Y.;Xiao, Y.;Zhang, Q.;Zhao, T.;Liao, H.-G.;Hwang, I.;Sun, C.-J.;Amine, K.;Wang, Q.;Sun, Y.;Xu, G.-L.;Gu, L.;Qiao, Y.; Sun, S.-G. Sustainable layered cathode with suppressed phase transition for long-life sodium-ion batteries. Nat. Sustain. 2024, 7, 348-359.

[48] Zeng, G.; Zeng, L.; Tang, Y.; Wu, Y.; Li, L.; Li, C.; Wang, Q.; Yang, M.; Qiao, Y.; Sun, S. Gliding-Induced Stacking Faults in Layered Oxide Cathode. J. Am. Chem. Soc. 2026, 118, 36983–36996.

[49] Jin, J.;Liu, Y.;Shen, Q.;Zhao, X.;Zhang, J.;Song, Y.;Li, T.;Xing, X.; Chen, J. Unveiling the Complementary Manganese and Oxygen Redox Chemistry for Stabilizing the Sodium-Ion Storage Behaviors of Layered Oxide Cathodes. Adv. Funct. Mater. 2022, 32, 2203424.

[50] Konarov, A.;Jo, J. H.;Choi, J. U.;Bakenov, Z.;Yashiro, H.;Kim, J.; Myung, S.-T. Exceptionally highly stable cycling performance and facile oxygen-redox of manganese-based cathode materials for rechargeable sodium batteries. Nano Energy 2019, 59, 197-206.

Just Accepted



Yangyang Huang received the Ph.D degree from Tongji University in 2021. From 2021 to 2023, he conducted postdoctoral research at the College of Chemistry, University of Waterloo, Canada. He is a Researcher Professor at Institute of Luminescent Materials and Information Displays, School of Materials Science and Engineering, Huaqiao University. His research interest is mainly focused on key cathode materials for energy storage batteries.



Peng Wei received his B.S degree from China University of Mining and Technology in June 2016 and Ph.D. degree from Huazhong University of Science and Technology in June 2022. He is an Assistant Professor in the School of Materials Science and Engineering at Changzhou University. His research interests focus on new energy storage systems, especially sodium-ion batteries.



Han Liu received his Ph.D. degree from the Department of Materials Science and Engineering, City University of Hong Kong (CityUHK), in 2023. He subsequently joined Prof. Yang Ren's group in the Department of Physics at CityUHK as a postdoctoral fellow and is currently a Research Assistant Professor in the same department. His research interests focus on the design, synthesis and mechanistic understanding of key materials for high-performance lithium-ion, sodium-ion and zinc-ion batteries, including polymer/gel electrolytes, solid-state electrolyte systems and high-voltage cathode materials.



Zhanhua Wei received her B.S. and Ph.D. degrees from the Xiamen University and Hong Kong University of Science and Technology in 2011 and 2015, respectively. He then conducted postdoctoral research at the School of Physical and Mathematical Sciences, Nanyang Technological University, Singapore, from 2015 to 2016. In 2016, he joined the College of Materials Science and Engineering at Huaqiao University, where he is currently a Professor, doctoral supervisor and Dean of the College of Materials Science and Engineering and the International College of New Energy. His research interests focus on advanced energy materials and devices for energy and optoelectronic conversion.

Just Accepted

Electronic Supplementary Material

Ni-induced structural Spring Effect in high-performance Mn-Rich P2-Type Sodium Cathodes

Yangyang Huang[1,§], Qingyun Hu[2,§], Peng Wei[3] (✉), Zhiwei Hu[4], Han Liu[2] (✉), Yong Wang[5], Shiwen Wang[6], Pengcheng Wang[6], Linsen Li[5], Yang Ren[2], and Zhanhua Wei[1] (✉)

1 Xiamen Key Laboratory of Optoelectronic Materials and Advanced Manufacturing, Institute of Luminescent Materials and Information Displays, College of Materials Science and Engineering, Huaqiao University, Xiamen 361000, China
2 Department of Physics, JC STEM Lab of Energy and Materials Physics, City University of Hong Kong, Hong Kong 999077, China.
3 School of Materials Science and Engineering, Changzhou University, Changzhou 213164, China
4 Max Planck Institute for Chemical Physics of Solids, Nöthnitzer Strasse 40, 01187, Dresden, Germany
5 Department of Chemical Engineering, Shanghai Electrochemical Energy Devices Research Center, School of Chemistry and Chemical Engineering, Shanghai Jiao Tong University, Shanghai, China
6 Xiamen Key Laboratory of Lithium Battery Energy Storage Application Materials and Safety, Xiamen Hithium Energy Storage Technology Co., Ltd., Xiamen 361000, China

[§]*These authors contributed equally.*

Supporting information to https://doi.org/10.26599/NRE.2026.9120294.

Address correspondence to Peng Wei, weipeng@cczu.edu.cn; Han Liu, hliu238@cityu.edu.hk; Zhanhua Wei, weizhanhua@hqu.edu.cn

Just Accepted

Experimental Section

Materials Synthesis

NLM and NLNM were prepared by a traditional solid-state reaction using Na2CO3, Li2CO3, NiO, and Mn2O3 as the raw materials. The calculated starting materials, according to the corresponding stoichiometric ratios, were mixed using a mortar and pestle and then pressed into a pellet at 10 MPa. The pellets were sintered at 700 °C for 15 h in air and then cooled down naturally. The final products were immediately transferred into an Ar-filled glove box to avoid contact with moisture in the air.

Materials Characterization

Crystal structures of as-prepared samples were examined by using an XRD diffractometer (Bruker D8 Advance) with a Cu Ka radiation source. XRD Rietveld refinements were performed on GSAS software[1]. The soft x-ray absorption (SXAS) spectra of the O-K edge were collected on the 20 A beamline at the National Synchrotron Radiation Research Center (NSRRC) in Hsinchu, Taiwan. All the samples were transferred under proper protection in the tests. In-situ synchrotron XRD experiments were conducted at the Australian Synchrotron with λ= 0.7748 Å. SEM characterization was performed on a Zeiss Sigma 300VP, and EDX images were recorded via an Aztec X-Max 80. The XPS measurements were performed on American Thermo Fisher Scientific ESCALAB 250Xi.

Electrochemical Measurements

The electrodes were prepared by mixing 70 wt% active materials, 20 wt% Super P, and 10 wt% poly(vinylidene fluoride)

with N-methylpyrrolidone to form a slurry and pasted on Al foil, and then dried in a vacuum oven at 120 °C overnight. The mass loading of active material ranged from 3.5-4.0 mg/cm2. Coin-type cells (2025-type) were assembled in the Ar-filled glove box using NLM and NLNM as the cathode, sodium metal as the anode, and 1.0 M NaClO4 in PC/EC/DMC (1:1:1 weight) with 2% FEC (fluoroethylene carbonate) as the electrolyte. Whatman glass fiber (CF/A) filter was adopted as the separator. Pouch-type full-cell were assembled with hard carbon (Kuraray, Type-2) as the anode. The cathodes were prepared by mixing NLNM, super-P and PVDF in a 94: 3: 3 mass ratio and coating them onto aluminum foils. The cathode material mass loading was controlled at ~ 15 mg cm-2. The anodes were prepared by combining 92 wt.% hard carbon, 4 wt.% carbon black Super-P, and 4 wt.% PVDF, and then coating the slurry onto aluminum foils. The n/p ratio was controlled in the range of 1.14. A short-circuit process was applied to supplement extra sodium ion and the contact duration was set to 5 mins. The electrolyte used was 1.0 M NaPF6 in a mixture of PC:EMC:FEC:PST:DTD in a volume ratio of 40:58:2:1:1. Galvanostatic cycling was carried out at room temperature using a NEWARE test system. The Galvanostatic intermittent titration technique (GITT) measurements were performed on a Land battery testing system, where the cell was charged/discharged at a current density of 10 mA/g with 50 min relaxation for each 10 min GITT pulse.

Calculation methods

All calculations in this study were performed with the Vienna ab-initio Simulation Package (VASP)[2] within the framework of density functional theory (DFT). The exchange-correlation interactions of the electron were described via the generalized gradient approximation (GGA) with PBE[3] functional, and the projector augmented wave (PAW) method[4] was used to describe the interactions of electron and ion. The kinetic energy cut-off of 500 eV was chosen for the plane wave expansion and the Monkhorst-Pack scheme with a 2x2x2 k-point mesh was used for the integration in the irreducible Brillouin zone. All calculations were spin polarized, and the DFT+U[5] method was used to treat the localized 3d electrons of Mn and Ni with U of 3.8 and 4, respectively[6]. The lattice parameters and ionic position were fully relaxed, and the total energy was converged within 10-5 eV per formula unit. The final forces on all ions are less than 0.02/Å. Density of states calculations were smeared by the Gaussian smearing method with a smearing width of 0.02 eV. The climbing-image nudged elastic band (CI-NEB) method[7, 8] was employed to evaluate the migration barriers of Na^+ and Li^+ in NLM and NLNM. For intralayer Na^+ migration, the initial and final configurations were constructed by placing Na^+ at two neighboring accessible sites within the Na layer. For interlayer Li^+ migration, Li^+ was initially located in the transition-metal layer and subsequently transferred to a neighboring vacant Na site in the adjacent Na layer. The migration pathways were constructed according to the local crystallographic connectivity and the accessibility of the destination sites. The same pathway-selection criteria were applied to NLM and NLNM to ensure a consistent comparison of the calculated migration barriers. All computations were performed on Sugon HPC clusters equipped with HYGON X86 32-core processors (2.5 GHz).

Table S1. Crystallographic parameters of NLNM refined with the Rietveld method.

Space Group			P63/mmc		
Atom	Site	x	y	z	Occ.
Na1	2b	0.0	0.0	0.25	0.2603
Na2	6h	0.6667	0.3333	0.25	0.5021
Ni	2a	0.0	0.0	0.0	0.1014
Li	2a	0.0	0.0	0.0	0.1493
Mn	2a	0.0	0.0	0.0	0.7492
O	12k	0.6667	0.3333	0.094	1.0
a = 2.8703 Å, c = 11.10 Å				wRp=3.91%	

Just Accepted

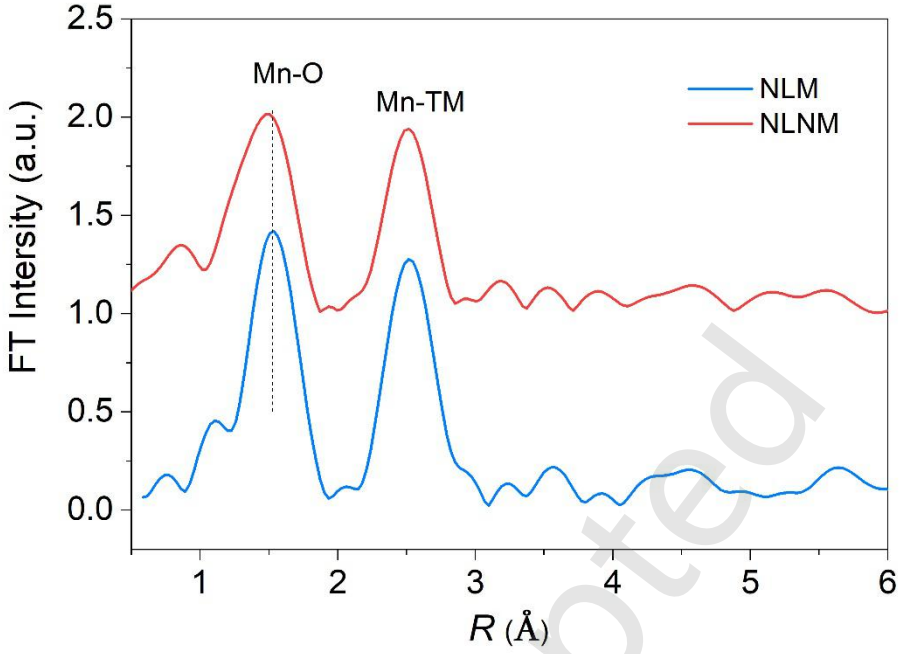


Figure S1. EXAFS spectra of Mn K-edge for NLM and NLNM.

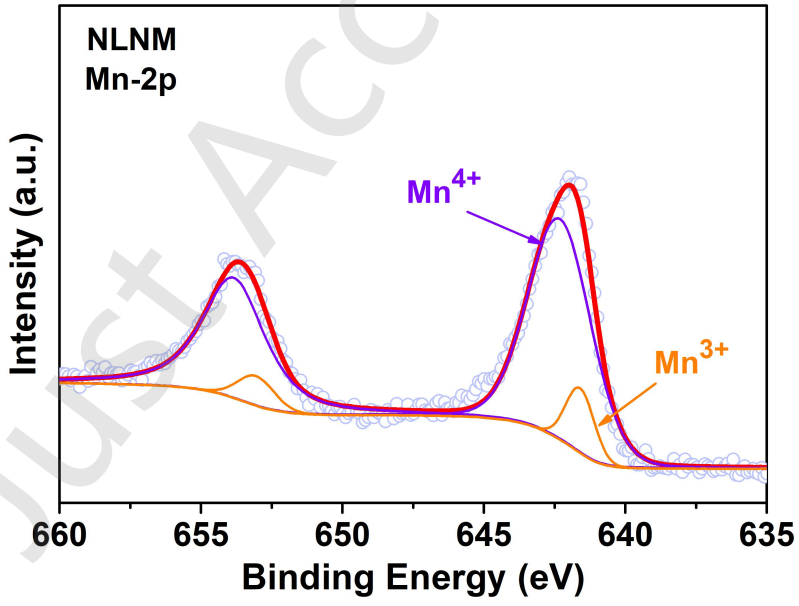


Figure S2. High-resolution XPS spectrum of Mn 2p of NLNM.

Just Accepted

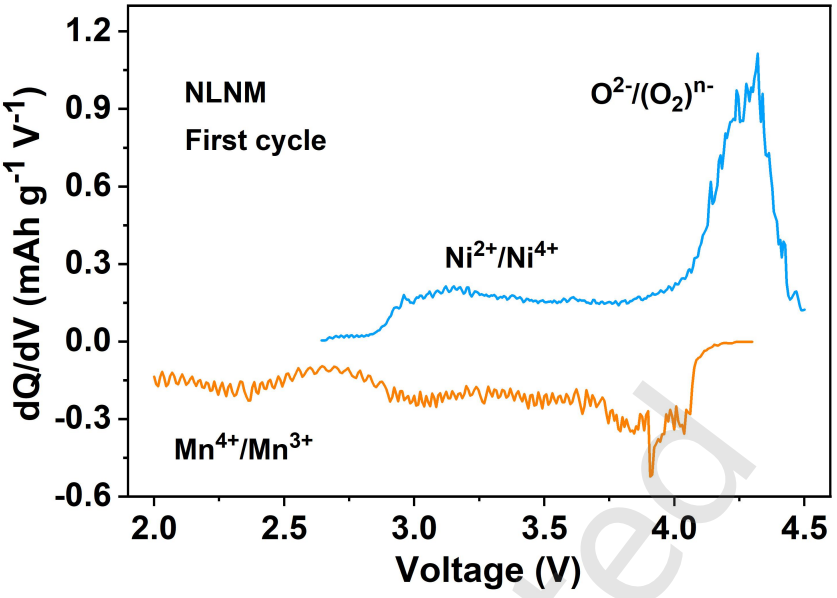


Figure S3. The dQ/dV curves of NLNM.

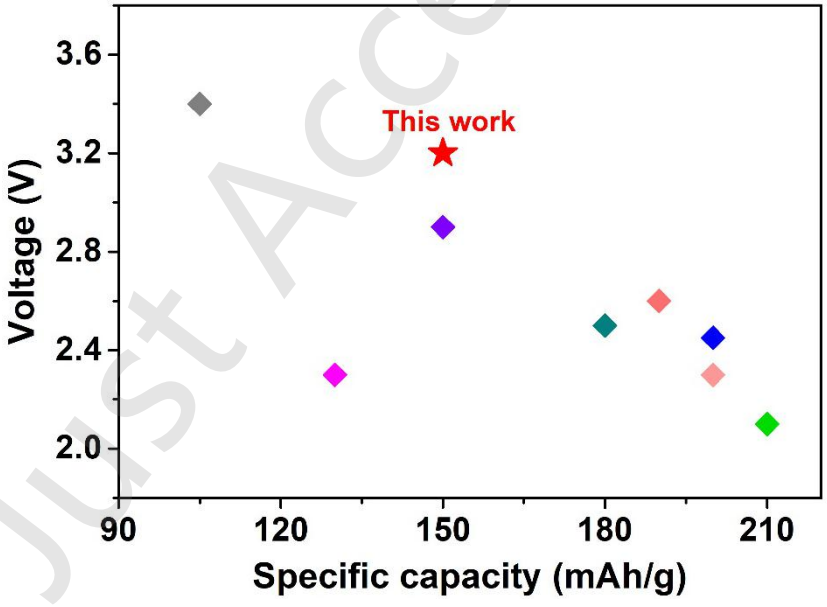


Figure S4. Comparison of the voltage and capacity of this work with those reported works.

Just Accepted

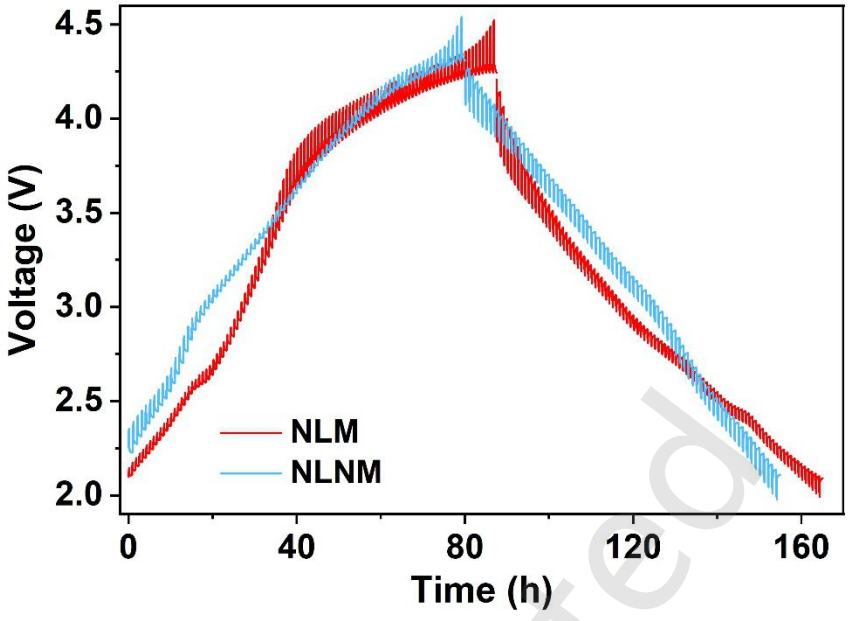


Figure S5. GITT profiles of NLM and NLNM.

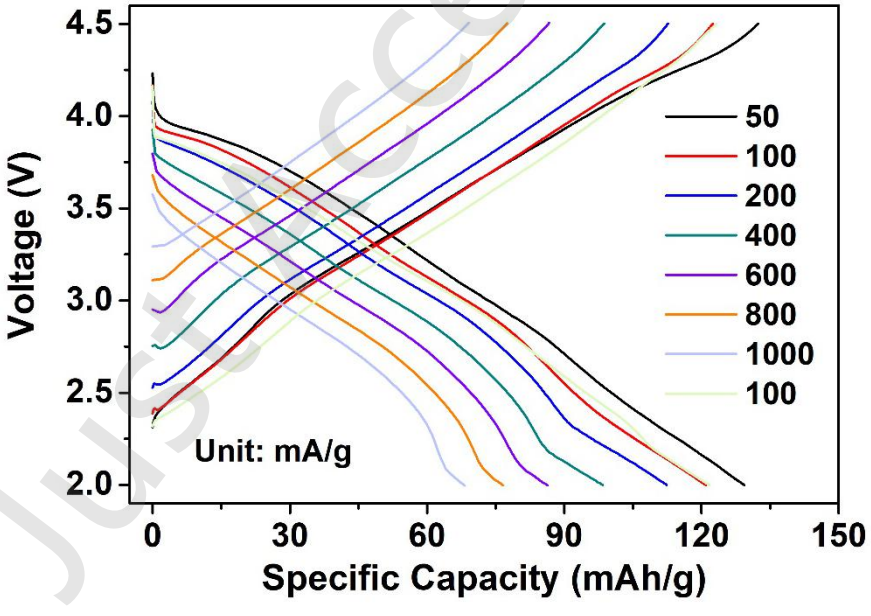


Figure S6. Charge/discharge profiles of NLNM at various current densities.

Just accepted

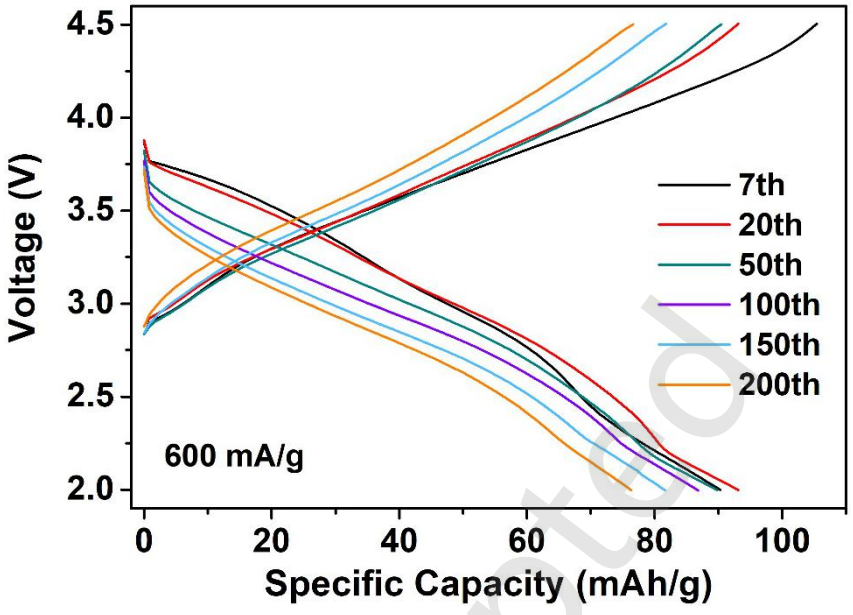


Figure S7. Charge/discharge profiles of NLNM at 600 mA/g.

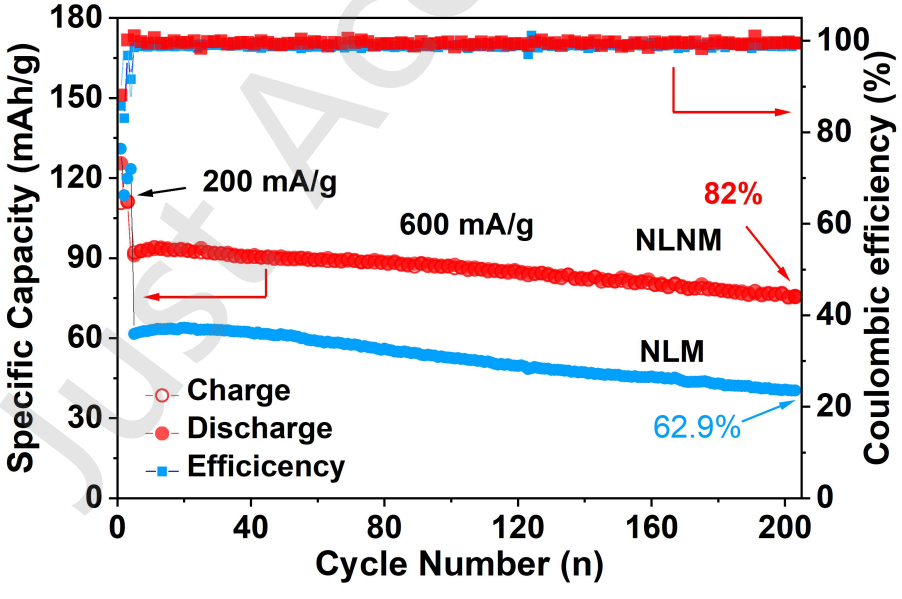


Figure S8. Cycling performance of NLM and NLNM at 600 mA/g.

Just Accepted

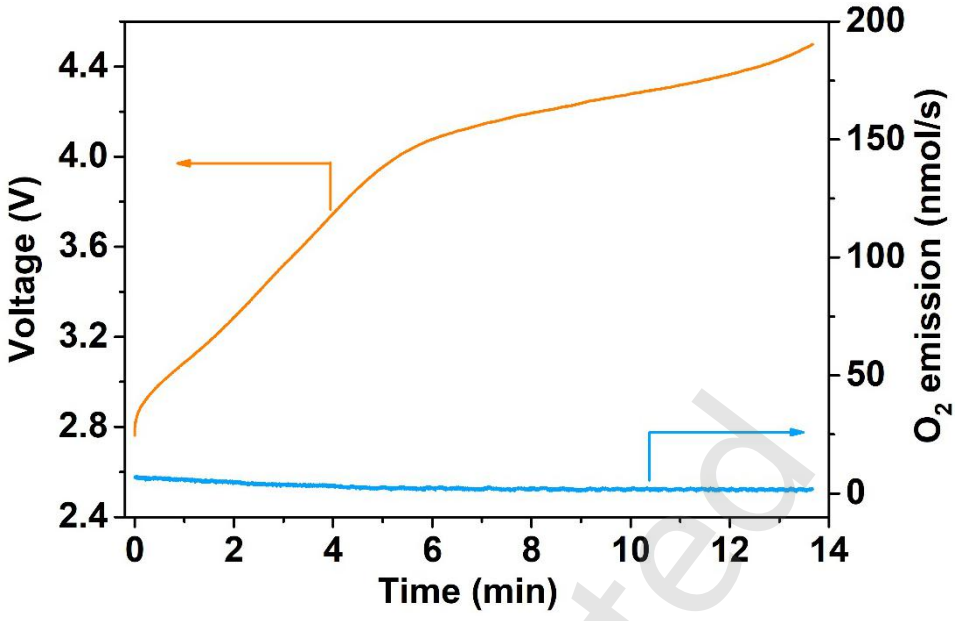


Figure S9. In situ DEMS results of gas evolution rates of O2.

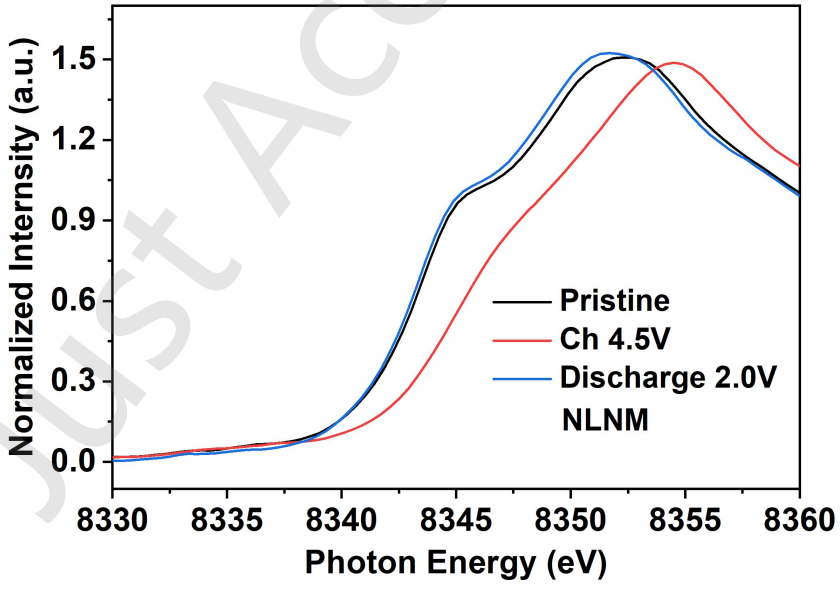


Figure S10. Ex-situ XANES spectra of Ni K-edge for NLNM.

Just Accepted

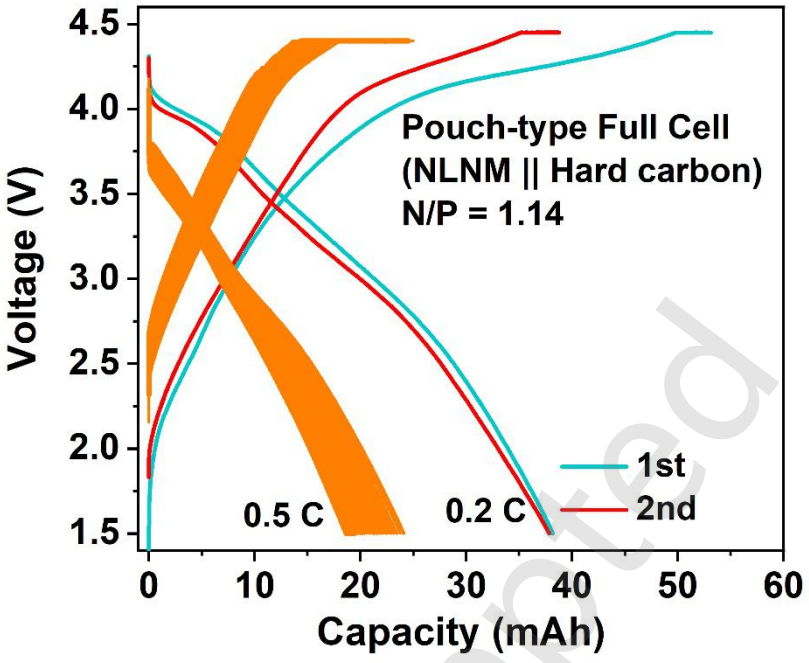


Figure S11. The typical charge/discharge profiles at different cycles of Pouch-type full cell of NLNM||HC.

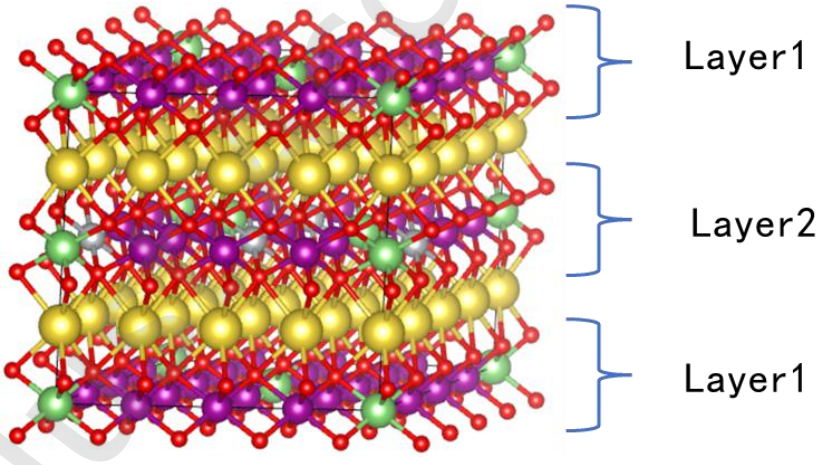


Figure S12. Schematic illustration of crystal structure for NLNM with layer 1 and 2.

Just accepted

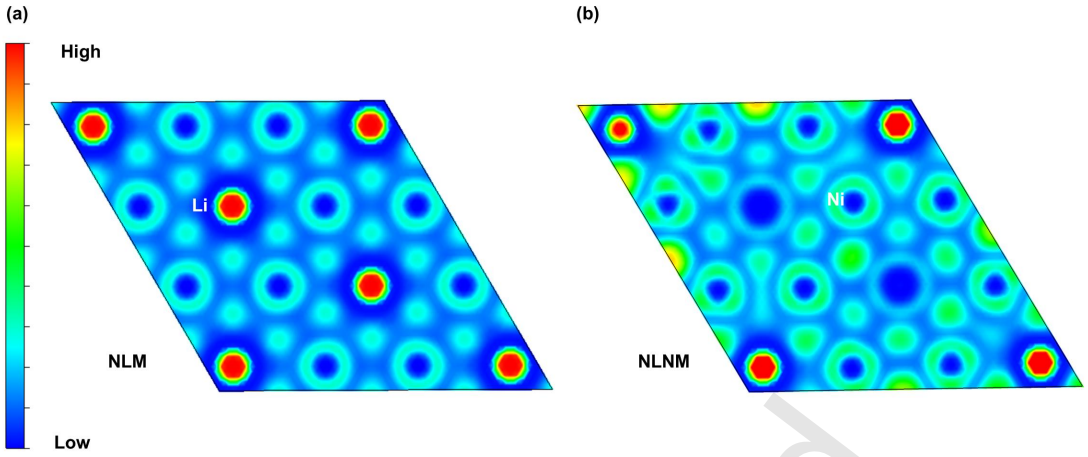


Figure S13. 2D slices of electron localization function (ELF) of valence electrons of (a) NLM and (b) NLNM.

Table S2. Mn_NLM-Pristine.

S1	0.26628
S2	0.22347
Det R1	-0.06013
Det R2	-0.01694
R1	1.968 (Mn-O)
R2	2.885 (Mn-Mn)

Table S3. Mn-NLNM-Pristine.

S1	0.28553
S2	0.23793
Det R1	-0.07492
Det R2	-0.00035
R1	1.968 (Mn-O)
R2	2.885 (Mn-Mn)

Table S4. Mn_NLM-4.5V

S1	1.7559
S2	S1*0.39
Det R1	-0.02224
Det R2	-0.17926
R1	1.968 (Mn-O)
R2	1.968 (Mn-O)

Just Accepted

Table S5. Mn-NLNM-4.5V

S1	0.28553
S2	S2*0.188
Det R1	-0.04873
Det R2	-0.1978
R1	1.968 (Mn-O)
R2	1.968 (Mn-O)

References:

[1] Toby, B. H. EXPGUI, a graphical user interface forGSAS. J. Appl. Crystallogr. 2001, 34, 210-213.

[2] G. Kresse, J. F. Efficient Iterative Schemes for Ab Initio Total-Energy calculations Using a Plane-Wave Basis Set. Phys. Rev. B. 1996, 54, 11169-11186.

[3] G. Kresse, D. J. From ultrasoft pseudopotentials to the projector augmented-wave method. Phys. Rev. B. 1999, 59, 1758-1775.

[4] John P. Perdew, K. B., Matthias Ernzerhof Generalized Gradient Approximation Made Simple. Phys. Rev. Lett. 1996, 77, 3865–3868.

[5] Monkhorst, H. J.; Pack, J. D. Special points for Brillouin-zone integrations. Physical Review B 1976, 13, 5188-5192.

[6] Anisimov, V. V.;Zaanen, J.; Andersen, O. K. Band theory and Mott insulators: Hubbard U instead of Stoner I. Phys Rev B Condens Matter 1991, 44, 943-954.

[7] Smidstrup, S.;Pedersen, A.;Stokbro, K.; Jonsson, H. Improved initial guess for minimum energy path calculations. J. Chem. Phys. 2014, 140, 214106.

[8] Henkelman, G.;Uberuaga, B. P.; Jónsson, H. A climbing image nudged elastic band method for finding saddle points and minimum energy paths. The Journal of Chemical Physics 2000, 113, 9901-9904.

Just Accepted